DES Y1 Results: validating cosmological parameter estimation using simulated Dark Energy Surveys

N. MacCrann,[1,2]⋆ J. DeRose,[3,4]⋆ R. H. Wechsler,[3,4,5] J. Blazek,[1,6] E. Gaztanaga,[7,8]
M. Crocce,[7,8] E. S. Rykoff,[4,5] M. R. Becker,[3,4] B. Jain,[9] E. Krause,[10,11] T. F. Eifler,[10,11]
D. Gruen,[4,5]† J. Zuntz,[12] M. A. Troxel,[1,2] J. Elvin-Poole,[13] J. Prat,[14] M. Wang,[15]
S. Dodelson,[16] A. Kravtsov,[17] P. Fosalba,[7,8] M. T. Busha,[4] A. E. Evrard,[18,19]
D. Huterer,[19] T. M. C. Abbott,[20] F. B. Abdalla,[21,22] S. Allam,[15] J. Annis,[15] S. Avila,[23] G.
M. Bernstein,[9] D. Brooks,[21] E. Buckley-Geer,[15] D. L. Burke,[4,5] A. Carnero Rosell,[24,25]
M. Carrasco Kind,[26,27] J. Carretero,[14] F. J. Castander,[7,8] R. Cawthon,[17] C. E. Cunha,[4] C.
B. D'Andrea,[9] L. N. da Costa,[24,25] C. Davis,[4] J. De Vicente,[28] H. T. Diehl,[15] P. Doel,[21]
J. Frieman,[15,17] J. García-Bellido,[29] D. W. Gerdes,[18,19] R. A. Gruendl,[26,27]
G. Gutierrez,[15] W. G. Hartley,[21,30] D. Hollowood,[31] K. Honscheid,[1,2] B. Hoyle,[32,33]
D. J. James,[34] T. Jeltema,[31] D. Kirk,[21] K. Kuehn,[35] N. Kuropatkin,[15] M. Lima,[36,24]
M. A. G. Maia,[24,25] J. L. Marshall,[37] F. Menanteau,[26,27] R. Miquel,[38,14] A. A. Plazas,[11]
A. Roodman,[4,5] E. Sanchez,[28] V. Scarpine,[15] M. Schubnell,[19] I. Sevilla-Noarbe,[28]
M. Smith,[39] R. C. Smith,[20] M. Soares-Santos,[40] F. Sobreira,[41,24] E. Suchyta,[42]
M. E. C. Swanson,[27] G. Tarle,[19] D. Thomas,[23] A. R. Walker,[20] J. Weller[43,32,33] and
DES Collaboration

Affiliations are listed at the end of the paper

Accepted 2018 July 13. Received 2018 June 17; in original form 2018 March 26

ABSTRACT

We use mock galaxy survey simulations designed to resemble the Dark Energy Survey Year 1 (DES Y1) data to validate and inform cosmological parameter estimation. When similar analysis tools are applied to both simulations and real survey data, they provide powerful validation tests of the DES Y1 cosmological analyses presented in companion papers. We use two suites of galaxy simulations produced using different methods, which therefore provide independent tests of our cosmological parameter inference. The cosmological analysis we aim to validate is presented in DES Collaboration et al. (2017) and uses angular two-point correlation functions of galaxy number counts and weak lensing shear, as well as their cross-correlation, in multiple redshift bins. While our constraints depend on the specific set of simulated realisations available, for both suites of simulations we find that the input cosmology is consistent with the combined constraints from multiple simulated DES Y1 realizations in the $\Omega_m - \sigma_8$ plane. For one of the suites, we are able to show with high confidence that any biases in the inferred $S_8 = \sigma_8(\Omega_m/0.3)^{0.5}$ and Ω_m are smaller than the DES Y1 $1 - \sigma$ uncertainties. For the other suite, for which we have fewer realizations, we are unable to be this conclusive; we infer a roughly 60 per cent (70 per cent) probability that systematic bias in the recovered Ω_m (S_8) is sub-dominant to the DES Y1 uncertainty. As cosmological analyses of this kind become increasingly more precise, validation of parameter inference using survey simulations will be essential to demonstrate robustness.

⋆ E-mail: maccrann.2@osu.edu (NM); jderose@stanford.edu (JD)
† Einstein fellow.

Key words: large-scale structure of Universe – cosmological parameters.

1 INTRODUCTION

The combination of our best cosmological data sets and our best theory of gravity supports our bizarre standard cosmological model: a Universe dominated by dark energy and dark matter. Dark energy is required to produce the observed acceleration of the Universe's expansion, and current observational constraints are consistent with the description of dark energy as a cosmological constant, Λ. In general, cosmological probes are sensitive to the properties of dark energy either because of its effect on the Universe's background properties (e.g. expansion rate, or average matter density as a function of cosmic time), or its effect on the growth of structure (or both). While some early indications that our Universe is not matter-dominated came from galaxy clustering measurements sensitive to the latter (e.g. Maddox, Efstathiou & Sutherland 1996), arguably the most robust evidence for ΛCDM (Λ + cold dark matter) comes from cosmological probes which are primarily sensitive to the former, known as *geometrical probes*. The most mature of these are the distance–redshift relation of Type 1a supernovae (SN1a, e.g. Betoule et al. 2014), and the baryon acoustic peaks in the cosmic microwave background (e.g. Planck Collaboration et al. 2015) and galaxy distributions (e.g. Alam et al. 2017; Ross et al. 2017). Indeed, the SN1a analyses of Perlmutter et al. (1999) and Riess et al. (1998) are considered the first convincing evidence of the Universe's late-time acceleration.

The development of more powerful probes of the growth of structure, as well as providing tighter constraints on the vanilla ΛCDM model, are likely to be extremely useful for constraining deviations from ΛCDM (e.g. Albrecht et al. 2006; Weinberg et al. 2013), for example, models with time-evolving dark energy and modified gravity, especially when combined with geometrical probes. Several observational programs are underway (The Dark Energy Survey[1] (DES), The Kilo-Degree Survey[2] (KiDS), The Hyper Suprime-Cam Subaru Strategic Survey[3]) that are designed to provide imaging in the optical and near infra-red that is sufficiently deep, wide, and high quality to enable competitive cosmological information to be extracted from the Universe's large-scale structure at $z < 2$. Meanwhile, future surveys carried out by the Large Synoptic Survey Telescope[4] (LSST), Euclid[5], and the Wide-Field Infrared Survey Telescope[6] will enable order-of-magnitude improvements in cosmological constraints if systematic uncertainties can be controlled sufficiently.

Much of the information on structure growth available to these surveys lies well beyond the linear regime, so making theoretical predictions to capitalize on this information is challenging, because of computational expense (large N-body simulations are required), and because there exists theoretical uncertainty on how to implement the baryonic physics that affects the matter distribution on small scales (Vogelsberger et al. 2014; Schaye et al. 2015). Further modelling challenges arise when objects such as galaxies or clusters are used as tracers of the underlying matter field, since this requires understanding the statistical connection between these objects and the matter field. Cosmological simulations are crucial for tackling both of these challenges, and are already widely used to predict the clustering of matter on nonlinear scales (e.g. Smith et al. 2003; Heitmann et al. 2010). Some recent works have used cosmological simulations to directly make predictions for galaxy clustering statistics (e.g. Kwan et al. 2015; Sinha et al. 2017).

The complexity of the analyses required to extract unbiased cosmological information from current and upcoming large-scale structure surveys demands thorough validation of the inference of cosmological parameters. Inevitably, approximations will be made in the model, for example to allow for fast likelihood evaluation in Markov chain Monte Carlo (MCMC) chains. While the impact of many of these can be investigated analytically (for example the impact of making the Limber approximation, or ignoring the effect of lensing magnification on galaxy clustering statistics), this requires the investigators to identify and characterize all of these effects (and possibly their interactions) with sufficient accuracy. It would be complacent to ignore the possibility that some of these effects may slip through the net.

The modelling challenges described will be entangled with challenges related to the quality of the observational data such as spatially correlated photometric and weak lensing shear estimation errors, and photometric redshift uncertainties. It has been recognized that analysis of realistic survey simulations, which can naturally contain many of the theoretical and observational complexities of real survey data, will play a crucial part in this validation, for example both the Dark Energy Spectroscopic Instrument and LSST Dark Energy Science collaborations plan to complete a series of simulated data challenges before analysis of real survey data (e.g. LSST Dark Energy Science Collaboration 2012). This is an especially powerful approach when one considers the importance of performing a blind analysis of the real survey data – ideally one can finalize all analysis choices, informed by analysis of the survey simulations, before the analysis of the real data.

In this spirit, we use mock survey simulations for this task by attempting to recover the input cosmological parameters of the simulations using a methodology closely resembling that used on the real DES Year 1 (Y1) data in DES Collaboration et al. (2017). We note that since we are not directly using these simulations to provide theoretical predictions for the analysis of the real data, having simulations which match the properties of the real data in every aspect is not essential, although, of course the more realistic the simulations are, the more valuable the validation they provide. The simulations used in this work reflect the current state of the survey simulations used in the Dark Energy Survey, and are being improved as the survey progresses; we discuss some potential improvements in Section 6. One of the challenges of such an analysis is disentangling biases in the inferred cosmological parameters caused by flaws in the inference process from those caused by features of the simulations that may not reflect the actual Universe. In this work, we limit the amount of validation of the simulations themselves, in an effort to produce results on a similar time-scale as the analyses of real DES Y1 data.

This work considers two of the observables provided by galaxy imaging surveys: the weak gravitational lensing shear, and the galaxy number density. Probes of the growth of structure can be thought of as those which depend on the clustering statistics of the Universe's matter field; both the galaxy number density and the shear meet this requirement. Weak gravitational lensing is the

---

[1] https://www.darkenergysurvey.org
[2] http://kids.strw.leidenuniv.nl
[3] http://www.subarutelescope.org/Projects/HSC
[4] http://www.lsst.org
[5] http://sci.esa.int/science-e/www/area/index.cfm?fareaid=102
[6] http://wfirst.gsfc.nasa.gov

observed distortion of light emitted from distant sources by variations in the gravitational potential due to intervening structures. In galaxy imaging data, this manifests as distortions in the observed size, brightness, and ellipticity of distant galaxies, which are referred to as *source* galaxies. The ellipticity distortion is known as the *shear*, and is the most commonly used weak lensing observable in galaxy surveys.

Since the shear field depends on the projected matter density field (as well as the redshift of the source galaxies and the distance–redshift relation), its *N*-point statistics are directly sensitive to the *N*-point statistics of the intervening density field and the cosmological parameters that determine these. Cosmic shear alone can therefore provide competitive cosmological constraints (Bartelmann & Schneider 2001; Kilbinger 2015; Troxel et al. 2017). Here, we consider two-point shear correlations, which are primarily sensitive to the two-point correlation function of the matter over-density $\xi_{mm}(r)$.

Galaxies, meanwhile are assumed to reside in massive gravitationally bound clumps of matter often modelled as halos (spherical or ellipsoidal overdensities in the matter field). Thus, while galaxies trace the matter field (i.e. they are generally more likely to be found where there is more mass), they do so in a biased way: the overdensity (the fractional excess with respect to the mean) in number of galaxies at **x** is not the same as the overdensity in matter at **x**. However, on sufficiently large scales, we can assume linear biasing, such that the two-point correlation function of galaxies, $\xi_{gg}(r)$, can be related to the matter two-point correlation function via (e.g. Fry & Gaztanaga 1993)

$$\xi_{gg}(r) = b_1^2 \xi_{mm}(r). \tag{1}$$

The constant of proportionality, b_1, is known as the *galaxy bias*, and depends on details of galaxy formation that most cosmological analyses do not attempt to model from first principles, instead leaving bias as a free nuisance parameter. In this case, galaxy clustering measurements alone (at least in the linear bias regime), do not provide strong constraints on the cosmologically sensitive matter clustering amplitude – some other information is required to break the degeneracy with the galaxy bias.

The cross-correlation between galaxy number density and shear, also known as as *galaxy–galaxy lensing*, can provide this information. It depends on the galaxy–matter cross-correlation, which in the linear bias regime can also be related to ξ_{mm} via

$$\xi_{gm}(r) = b_1 \xi_{mm}(r). \tag{2}$$

Hence, galaxy clustering and galaxy-shear cross-correlations depend on complementary combinations of the galaxy bias and ξ_{mm}, and can be combined to allow useful cosmological inference (e.g. Mandelbaum et al. 2013; Kwan et al. 2017).

This work is a companion to a cosmological parameter estimation analysis of Dark Energy Survey Year 1 (DES Y1) data, in which we use the three aforementioned two-point signals: cosmic shear, galaxy clustering, and galaxy-galaxy lensing to infer cosmological parameters and test cosmological models (DES Collaboration et al. 2017). Further details on the cosmic shear, galaxy clustering, and galaxy-galaxy lensing parts of the analysis are available in Troxel et al. (2017), Elvin-Poole et al. (2017), and Prat et al. (2017), respectively. These are therefore the statistics we measure and model from the survey simulations considered in this work, in an attempt to demonstrate robust cosmological parameter inference.

In Section 2, we describe the statistics estimated from the data, and how they are modelled. In Section 3, we describe the suites of simulations used. In Section 4, we describe the galaxy samples used. In Section 5, we present the correlation function measure-

ments, our analysis choices (which closely follow those which are used on the real data in DES Collaboration et al. 2017), and our inferred cosmological parameters. We also test the robustness of the constraints to photometric redshift errors. We conclude with a discussion in Section 6.

2 TWO-POINT STATISTICS

We construct two galaxy samples – one suited to estimating galaxy number density, and the other suited to estimating shear. We will refer to the galaxy sample used to estimate number density as the *lens* sample, and that used to estimate shear as the *source* sample. From these two samples, we construct three types of angular correlation functions - the auto-correlation of counts of the lens sample (galaxy clustering), the auto-correlation of the shear of the source sample (cosmic shear), and the cross-correlation between counts of the lens sample and shear of the source sample (galaxy–galaxy lensing).

The galaxy clustering statistic we use is $w(\theta)$, the excess number of galaxy pairs separated by angle θ over that expected from randomly distributed galaxies, estimated using the optimal and unbiased estimator of Landy & Szalay (1993). Meanwhile, the information in galaxy–galaxy lensing is well-captured by the mean *tangential shear*, $\langle \gamma_t(\theta) \rangle$ ($\gamma_t(\theta)$ henceforth), the tangential component of the shear with respect to the lens–source separation vector, averaged over all lens–source pairs separated by angle θ. In our estimation of the tangential shear, we include the subtraction of the tangential shear signal around points randomly sampled from the survey window function of the lens sample, which reduces the effects of additive shear biases (e.g. Hirata et al. 2004) and cosmic variance (Singh et al. 2017).

Since shear is a spin-2 field, one requires three two-point correlation functions to capture the two-point information of the shear field. One could use auto-correlations of the shear component tangential to the separation vector, $C_{++}(\theta)$, auto-correlations of the shear at $45°$ to the separation vector, $C_{\times\times}(\theta)$, and the cross-correlation $C_{+\times}(\theta)$. In practice, $C_{+\times}(\theta)$ vanishes by parity arguments and we use the linear combinations of the remaining two correlations functions $\xi_\pm(\theta) = C_{++}(\theta) \pm C_{\times\times}(\theta)$.

We split both lens and source galaxies into multiple bins in redshift, and measure correlation functions $\zeta^{ij}(\theta) \in \left\{ w^{ij}(\theta), \gamma_t^{ij}(\theta), \xi_+^{ij}(\theta), \xi_-^{ij}(\theta) \right\}$ between redshift bins i and j.

We use superscripts in the following to denote quantities relating to a particular redshift bin, so they should not be interpreted as exponents. In general, an angular correlation function $\zeta_{\alpha\beta}^{ij}(\theta)$, can be related to a corresponding projected angular power spectrum, $C_{\alpha\beta}^{ij}(l)$ via

$$\zeta_{\alpha\beta}^{ij}(\theta) = \sum_l \frac{2l+1}{4\pi} C_{\alpha\beta}^{ij}(l) d_{mn}^l(\theta), \tag{3}$$

where α and β represent the two quantities being correlated (galaxy overdensity δ_g or shear γ), and $d_{nm}^l(\theta)$ is the Wigner D-matrix. For the galaxy correlation function, $w(\theta)$, $m = n = 0$, and the Wigner-D matrix reduces to the Legendre polynomial $P_l(\cos\theta)$. For the tangential shear, $\gamma_t(\theta)$, $m = 2$ and $n = 0$, and the Wigner-D matrix reduces to the associated Legendre polynomial $P_l^2(\cos\theta)$. For the shear correlation functions $\xi_\pm(\theta)$, $m = 2$ and $n = \pm2$; the Wigner D-matrices in this case can also be written in terms of associated Legendre polynomials (see Stebbins 1996 for the somewhat lengthy expressions).

In the small-angle limit, equation (3) can be approximated with a Hankel transform

$$\zeta_{\alpha\beta}^{ij}(\theta) = \int dl \, l \, C_{\alpha\beta}^{ij}(l) J_n(\theta), \qquad (4)$$

where $n = 0$ for $w(\theta)$, $n = 2$ for $\gamma_t(\theta)$, $n = 0$ for $\xi_+(\theta)$ and $n = 4$ for $\xi_-(\theta)$. Krause et al. (2017) demonstrate that this approximation is sufficient for this analysis at the accuracy of DES Y1.

The angular power spectra, $C_{\alpha\beta}^{ij}(l)$ can be expressed in terms of the corresponding three-dimensional power spectra $P_{\alpha\beta}(k)$ as (LoVerde & Afshordi 2008)

$$C_{\alpha\beta}^{ij}(l) = \int_0^{\chi_h} d\chi \, D_A^{-1}(\chi) f_\alpha^i(\chi) J_{l+1/2}(k\chi)$$
$$\int_0^{\chi_h} d\chi' \, D_A^{-1}(\chi') f_\beta^j(\chi') J_{l+1/2}(k\chi')$$
$$\int_0^\infty dk k P_{\alpha\beta}(k, \chi, \chi'). \qquad (5)$$

χ is the comoving radial distance, $D_A(\chi)$ is the comoving angular diameter distance, χ_h is the horizon distance, and $f_\alpha^i(\chi)$ and $f_\beta^i(\chi')$ are the appropriate projection kernels for computing the projected shear or number counts in redshift bin i from the shear or number counts in three dimensions.

Under the Limber approximation (Limber 1953), equation (5) is simplified to

$$C_{\alpha\beta}^{ij}(l) = \int_0^{\chi_h} d\chi \, \frac{f_\alpha^i(\chi) f_\beta^i(\chi)}{D_A^2(\chi)} P_{\alpha\beta}(k = (l + 1/2)/\chi, \chi). \qquad (6)$$

Predictions for each of the two-point correlation functions that we use can therefore be derived using equations (4) and (6) (in the flat-sky and Limber approximations); once we specify the appropriate power spectrum, $P_{\alpha\beta}(k, \chi)$, and two radial kernels, $f_\alpha^i(\chi)$ and $f_\beta^i(\chi)$. For galaxy number counts, the projection kernel, $f_{\delta_g}(\chi)$ is simply the comoving distance probability distribution of the galaxy sample (in this case the lens sample) $n_{\text{lens}}^i(\chi)$, normalized so that $\int d\chi \, n_{\text{lens}}^i(\chi) = 1$. For shear, the projection kernel for redshift bin i is

$$f_\gamma^i(\chi) = \frac{3 H_0^2 \Omega_m D_A(\chi)}{2 c^2 a(\chi)} \int_0^{\chi_h} d\chi' n_{\text{src}}^i(\chi) \frac{D_A(\chi' - \chi)}{D_A(\chi')}, \qquad (7)$$

where $n_{\text{src}}^i(\chi)$ is the comoving distance probability distribution of the source galaxies.

It follows that for $w^{ij}(\theta)$, the radial kernels are $n_{\text{lens}}^i(\chi)$ and $n_{\text{lens}}^j(\chi)$ and the power spectrum is the galaxy power spectrum, $P_{gg}^{ij}(k, \chi)$. In our fiducial model, we assume linear bias, and thus relate this to the matter power spectrum, $P_{mm}(k, z)$, via

$$P_{gg}^{ij}(k, z) = b_1^i b_1^j P_{mm}(k, z), \qquad (8)$$

where b_1^i is a free linear galaxy bias parameter for redshift bin i, assumed to be constant over the redshift range of each lens redshift bin. In principle, there is also a shot noise contribution to the galaxy power spectrum. However, we neglect this term since any constant contribution to the power spectrum appears only at zero lag in the real-space statistics we use here, and we do not use measurements at zero-lag.

For $\gamma_t^{ij}(\theta)$, the radial kernels are $n_{\text{lens}}^i(\chi)$ and $f_\gamma^j(\chi)$, and the appropriate power spectrum is the galaxy–matter power spectrum $P_{gm}(k, \chi)$, which in the linear bias regime is given by

$$P_{gm}^{ij}(k, \chi) = b_1^i P_{mm}(k, \chi). \qquad (9)$$

Finally, for $\xi_\pm^{ij}(\theta)$, the radial kernels are $f_\gamma^i(\chi)$ and $f_\gamma^j(\chi)$, and the appropriate power spectrum is simply the matter power spectrum, $P_{mm}(k, \chi)$.

3 SURVEY SIMULATIONS

We now describe the two suites of simulations used in this work, which we will refer to as the *BCC* and *MICE*. The latter is already well-documented in Fosalba et al. (2015a), Carretero et al. (2015), and Fosalba et al. (2015b), hence we only include a brief description in Section 3.2. It will be useful in the following to note a few details of the DES Y1 dataset that is being simulated. The Year 1 dataset is constructed from DECam (Flaugher et al. 2015) images taken between August 2013 and February 2014 (see, e.g. Drlica-Wagner et al. 2017). An area of 1786 deg² was imaged in *grizY*, but the cosmology analyses (DES Collaboration et al. 2017; Elvin-Poole et al. 2017; Prat et al. 2017; Troxel et al. 2017) used only the contiguous 1321 deg² region known as "SPT" (Drlica-Wagner et al. 2017).

3.1 BCC simulations

We make use of a suite of 18 simulated DES Year 1 galaxy catalogues constructed from dark matter-only N-body lightcones and include galaxies with DES *griz* magnitudes with photometric errors appropriate for the DES Y1 data, shapes, ellipticities sheared by the underlying dark matter density field, and photometric redshift estimates. The N-body simulations were generated assuming a flat ΛCDM cosmology with $\Omega_m = 0.286$, $\Omega_b = 0.047$, $n_s = 0.96$, $h = 0.7$ and $\sigma_8 = 0.82$. A more detailed description of this suite of simulations will be presented in DeRose et al. (2018). These mocks are part of the ongoing 'blind cosmology challenge' effort within DES, and hence are referred to as the *BCC* simulations.

3.1.1 N-body simulations

For the production of large-volume mock galaxy catalogues suitable to model the DES survey volume, we use three different *N*-body simulations per each set of 6 DES Year 1 catalogues. Any cosmological simulation requires a compromise between volume and resolution; the use of three simulation boxes per lightcone is intended to balance the requirements on volume and resolution which change with redshift. At lower redshift, less volume is required for the same sky area compared to higher redshift, but higher resolution is required to resolve the excess nonlinear structure on a given comoving scale. Properties of the three simulations are summarized in Table 1. All simulations are run using the code L-Gadget2, a proprietary version of the Gadget-2 code (Springel 2005) optimized for memory efficiency and designed explicitly to run large-volume dark matter-only N-body simulations.

Additionally, we have modified this code to create a particle lightcone output on the fly. Linear power spectra computed with CAMB (Lewis 2004) were used with 2LPTic (Crocce, Pueblas & Scoccimarro 2006) to produce the initial conditions using second-order Lagrangian perturbation theory.

3.1.2 Galaxy model

Galaxy catalogues are built from the lightcone simulations using the ADDGALS algorithm. We briefly describe the algorithm, and refer

Table 1. Description of the N-body simulations used.

Simulation	box size	particle number	mass resolution	force resolution	halo mass cut
BCC ($0.00 < z < 0.34$)	$1.05\,h^{-1}$ Gpc	1400^3	$3.35 \times 10^{10}\,h^{-1}\,\mathrm{M_\odot}$	$20\,h^{-1}$ kpc	$3.0 \times 10^{12}\,h^{-1}\,\mathrm{M_\odot}$
BCC ($0.34 < z < 0.90$)	$2.60\,h^{-1}$ Gpc	2048^3	$1.62 \times 10^{11}\,h^{-1}\,\mathrm{M_\odot}$	$35\,h^{-1}$ kpc	$3.0 \times 10^{12}\,h^{-1}\,\mathrm{M_\odot}$
BCC ($0.90 < z < 2.35$)	$4.00\,h^{-1}$ Gpc	2048^3	$5.91 \times 10^{11}\,h^{-1}\,\mathrm{M_\odot}$	$53\,h^{-1}$ kpc	$2.4 \times 10^{13}\,h^{-1}\,\mathrm{M_\odot}$
MICE	$3.07\,h^{-1}$ Gpc	4096^3	$2.93 \times 10^{10}\,h^{-1}\,\mathrm{M_\odot}$	$50\,h^{-1}$ kpc	$\sim 10^{11}\,h^{-1}\,\mathrm{M_\odot}$

the reader to Wechsler et al. (2018) and DeRose et al. (2018) for more details.

The main strengths of this algorithm are its ability to reproduce the magnitude-dependent clustering signal found in subhalo abundance matching (SHAM) models, and its use of empirical models for galaxy spectral energy distributions (SEDs) to match colour distributions. SHAM models have been shown to provide excellent fits to observed clustering data (Conroy, Wechsler & Kravtsov 2006; Lehmann et al. 2017), thus by matching SHAM predictions, ADDGALS is able to accurately reproduce observed clustering measurements as well.

The ADDGALS algorithm can be subdivided into two main parts. First, using a SHAM on a high-resolution *N*-body simulation, we fit two independent parts of the galaxy model: $p(\delta|M_r, z)$, the distribution of matter overdensity, δ, given galaxy absolute magnitude, M_r, and redshift, z, and $p(M_{r,\,\mathrm{cen}}|M_{\mathrm{halo}}, z)$, the distribution of *r*-band absolute magnitude of central galaxies, $M_{r,\,\mathrm{cen}}$, given host halo mass, M_{halo}, and redshift. To do this, we subhalo abundance match a luminosity function $\phi(M_r, z)$, which has been constrained to match DES Y1 observed galaxy counts, to 100 different redshift snapshots and measure δ centered on every galaxy in the SHAM. The model for $p(\delta|M_r, z)$ is then fit to histograms of δ in narrow magnitude bins in the SHAM in each snapshot. The model for $p(M_{r,\,\mathrm{cen}}|M_{\mathrm{halo}}, z)$ is similarly constrained by fitting to the distributions of $M_{r,\,\mathrm{cen}}$ in bins of M_{halo} for each snapshot. Wechsler et al. (2018) shows that reproducing these distributions is sufficient to match the projected clustering found in the SHAM.

Now, using $\phi(M_r, z)$, $p(\delta|M_r, z)$ and $p(M_{r,\,\mathrm{cen}}|M_{\mathrm{halo}}, z)$, we add galaxies to our lightcone simulations. Working in redshift slices spanning $z_{\mathrm{low}} < z \leq z_{\mathrm{high}}$, we first place galaxies on every resolved central halo in the redshift shell, where the mass of a resolved halo, M_{min}, is given in Table 1, drawing its luminosity from $p(M_{r,\,\mathrm{cen}}|M_{\mathrm{halo}}, z)$. As these simulations are relatively low-resolution, this process only accounts for a few per cent of the galaxies that DES observes. For the rest, we create a catalogue of galaxies with absolute magnitudes $\{M_{r,\,i}\}$ and redshifts $\{z_i\}$, with $i = 1, \ldots, N$ and $N = \int_{z_{\mathrm{low}}}^{z_{\mathrm{high}}} dz \frac{dV}{dz} \phi_{\mathrm{unres}}(M_r, z)$, where

$$\phi_{\mathrm{unres}}(M_r, z) = \phi(M_r, z) - \phi_{\mathrm{res}}(M_r, z) \tag{10}$$

$$= \phi(M_r, z) \tag{11}$$

$$- \int_{M_{\mathrm{min}}}^{\infty} dM_{\mathrm{halo}}\, p(M_{r,cen}|M_{\mathrm{halo}}, z) n(M_{\mathrm{halo}}, z). \tag{12}$$

Each $M_{r,\,i}$ is drawn from $\phi_{\mathrm{unres}}(M_r, z_{\mathrm{mean}})$, where z_{mean} is the mean redshift of the slice, and each z_i is drawn uniformly between $z_{\mathrm{low}} < z_i \leq z_{\mathrm{high}}$. It can be shown that this uniform distribution is appropriate, since the distribution of particles in the lightcone already accounts for the change in comoving volume element as a function of redshift, $\frac{dV}{dz}$. Finally, in order to determine where to place each galaxy, we draw densities $\{\delta_i\}$ from $p(\delta|M_{r,\,i}, z_i)$, and assign the galaxies to particles in the lightcone with the appropriate density and redshift.

Notably, we make no explicit classification of galaxies as centrals or satellites when they are assigned in this way.

Once galaxies have been assigned positions and *r*-band absolute magnitudes, we measure the projected distance to their fifth nearest neighbour in redshift bins of width $\Delta z = 0.05$. We then bin galaxies in M_r and rank-order them in terms of this projected distance. We compile a training set consisting of the magnitude-limited spectroscopic SDSS DR6 VAGC cut to $z < 0.2$ and local density measurements from Cooper et al. (2006). This training set is rank-ordered the same way as the simulation. Rank-ordering the densities allows us to use a non-volume-limited sample in the data, since this rank is preserved under the assumption that galaxies of all luminosities are positively biased. Each simulated galaxy is assigned the SED from the galaxy in the training set with the closest density rank in the same absolute magnitude bin. The SED is represented as a sum of templates from Blanton et al. (2003), which can then be used to shift the SED to the correct reference frame and generate magnitudes in DES band passes. While the use of this training set neglects the evolution of the relationship between rank local density and SED between $z < 0.2$ and the higher redshifts probed by DES, it does provide a sample with high completeness over the required range of galaxy luminosity. The use of rank density should reduce the amount of redshift evolution in this relationship, but residual effects may be present in the colour-dependent clustering of the BCC simulations. While the agreement between red MaGiC angular clustering in the data and the BCC simulations is generally good, there are some redshift-dependent differences that could be partially attributable to this effect (DeRose et al. 2018). Planned improvements of the algorithm will take advantage of higher redshift spectroscopic data sets.

Galaxy sizes and ellipticities are assigned based on the galaxies' observed *i*-band magnitude based on fits to the joint distribution of these quantities in high-resolution Suprime-Cam data (Miyazaki et al. 2002).

3.1.3 Raytracing

In order to derive weak lensing quantities for each galaxy, we employ a multiple-plane raytracing algorithm called CALCLENS (Becker 2013). The raytracing is done on an $n_{\mathrm{side}} = 4096$ *HEALPIX* (Górski et al. 2005) grid, leading to an angular resolution of approximately $0.85'$. At each lens plane, the Poisson equation is solved using a spherical harmonic transform, thus properly accounting for sky curvature and boundary conditions. The inverse magnification matrix is interpolated from each ray at the centre of each lens plane to the correct angle and comoving distance of each galaxy. The magnitudes, shapes, and ellipticities of the galaxies are then lensed using this information.

3.1.4 Photometric errors and footprint

To create each of the BCC Y1 catalogues, a rotation is applied to the simulated galaxies to bring them into the DES Y1 SPT footprint

described in Section 3. The DES Y1 mask is applied and the area with $RA < 0$ is cut in order to fit 6 Y1 footprints into each simulation, leaving an area of $1122 \deg^2$ out of the original $1321 \deg^2$. Applying this cut allows us to use more area in each simulated half-sky (without the cut, we are only able to fit 2 Y1 footprints into each simulated half-sky without overlap), and therefore allows us to test our cosmological parameter inference with greater statistical precision. Photometric errors are applied to the *BCC* catalogues using the DES Y1 Multi-Object Fitting (*MOF*) depth maps. The errors depend only on the true observed flux of the galaxy and its position in the footprint, and not on its surface brightness profile.

3.2 MICE simulations

We use the MICE Grand Challenge simulation (MICE-GC), which is well-documented in Fosalba et al. (2015a); Carretero et al. (2015); Fosalba et al. (2015b); we provide a brief description here for convenience. MICE-GC constitutes a 3 Gpc h^{-1} N-body simulation with 4096^3 particles, produced using the Gadget-2 code (Springel 2005) as described in Fosalba et al. (2015b). The cosmological model is flat ΛCDM with $\Omega_m = 0.25$, $\Omega_b = 0.044$, $n_s = 0.95$, $h = 0.7$ and $\sigma_8 = 0.8$. The mass resolution is $2.93 \times 10^{10}\, h^{-1}\, \mathrm{M_\odot}$ and the force softening length is $50\, h^{-1}$ kpc. Halos are identified using a Friends-of-Friends algorithm (with linking length 0.2 times the mean inter-particle distance) and these are populated with galaxies via a hybrid sub-halo abundance matching (SHAM) and halo occupation distribution (HOD) approach (Carretero et al. 2015) designed to match the joint distributions of luminosity, $g - r$ color, and clustering amplitude observed in SDSS (Blanton et al. 2003; Zehavi et al. 2005). Weak lensing quantities are generated on a *HEALPIX* grid of $N_{\mathrm{side}} = 8192$ (an angular resolution of $\approx 0.4'$) assuming the Born approximation (see Fosalba et al. 2015a for details).

We rotate the MICE octant into the DES Y1 footprint and imprint the spatial depth variations in the real DES Y1 data onto the MICE galaxy magnitudes using the same method as for the BCC (see Section 3.1.4). We find we can apply two such rotations that retain the majority of the Y1 area and have little overlap in the Y1 area. Hence, we have two MICE-Y1 realizations.

3.3 Notable differences between the mock catalogues

We note the following significant differences between the mock catalogues constructed from the BCC and MICE simulations:

(i) Volume of data: We have 18 DES Y1 realizations for the BCC simulations, in principle allowing a measurement of any bias in the recovered cosmological parameters with uncertainty $1/\sqrt{18}$ of the DES Y1 statistical error. We note that the slightly smaller area used for the BCC simlations will result in a small loss of constraining power. For MICE on the other hand, we expect uncertainty on the recovered parameters that is more comparable to the DES Y1 statistical errors (a factor of $1/\sqrt{2}$ smaller). Ideally, the uncertainty on the inferred parameter biases should be subdominant to the achieved parameter constraint for DES Y1. Clearly what constitutes 'subdominant' is somewhat subjective, but we consider the 18 BCC realizations as satisfactory in this respect, while more MICE realizations would be desirable to satisfy this requirement.

(ii) Each BCC realization is constructed from three independent simulation boxes, resulting in discontinuities in the density field where they are joined together, while MICE uses a single box.

(iii) Resolution: The mass resolution of the lowest redshift BCC simulation box ($2.7 \times 10^{10}\, h^{-1}\, \mathrm{M_\odot}$) is similar to MICE ($2.93 \times$

$10^{10}\, h^{-1}\, \mathrm{M_\odot}$) with significantly higher force resolution, while the higher redshift boxes have signifcantly lower mass resolution (see Table 1) and comparable force resolution.

(iv) Galaxies are added to the N-body simulations using different methods (BCC uses ADDGALS, while MICE uses a hybrid SHAM and HOD approach); in general, this will lead to different galaxy bias behaviour in the non-linear regime.

(v) Weak lensing quantities in BCC are calculated using full ray-tracing, whereas in MICE they are calculated under the Born approximation. We do not, however expect this difference to be significant for the relatively large-scale observables considered here; indeed, we do not include beyond-Born approximation contributions in the theoretical modeling of the lensing signals used in our cosmological parameter inference.

(vi) For BCC, we use BPZ (Benítez 2000) photometric redshift estimates, the fiducial photo-z method used for the weak lensing source galaxies on the real DES Y1 data. For MICE, we use true redshifts for the weak lensing galaxies throughout.

4 GALAXY SAMPLES

We select two different galaxy samples from the mock catalogues, chosen based on their suitability to probe the galaxy number density (and act as the lens sample for the galaxy–galaxy lensing) and weak lensing shear fields, respectively.

4.1 Lens sample

To probe the galaxy number density, we use galaxies selected using the REDMAGIC algorithm (Rozo et al. 2016). REDMAGIC fits an empirically calibrated red-sequence template to all objects, and then selects those which exceed some luminosity threshold (assuming the photometric redshift inferred from the red-sequence template fit), and whose colours provide a good fit to the red-sequence template. This allows selection of a bright, red, galaxy sample with approximately constant comoving number density. The fact that they are close to the red sequence allows a high-quality photometric redshift (photo-z) estimation – the REDMAGIC galaxies used in the DES Y1 analyses (Elvin-Poole et al. 2017; DES Collaboration et al. 2017) have an average standard error, $\sigma_z = 0.017(1 + z)$. We refer to the photo-zs estimated by the REDMAGIC algorithm as z_{RM}.

As in Elvin-Poole et al. (2017) and DES Collaboration et al. (2017), we split the REDMAGIC sample into five redshift bins, defined $0.15 < z_{\mathrm{RM}} < 0.3$, $0.3 < z_{\mathrm{RM}} < 0.45$, $0.45 < z_{\mathrm{RM}} < 0.6$, $0.6 < z_{\mathrm{RM}} < 0.75$, $0.75 < z_{\mathrm{RM}} < 0.9$. For the first three redshift bins, the REDMAGIC *high-density* sample is used (luminosity, $L > 0.5L_*$; number density, $n_{\mathrm{gal}} = 4 \times 10^{-3}\, \mathrm{Mpc^{-3}}$), while the fourth and fifth redshift bins are selected from the high luminosity ($L > L_*$, $n_{\mathrm{gal}} = 1 \times 10^{-3}\, \mathrm{Mpc^{-3}}$) and higher luminosity ($L > 1.5L_*$, $n_{\mathrm{gal}} = 1 \times 10^{-4}\, \mathrm{Mpc^{-3}}$) samples, respectively. Selecting brighter galaxies at high-redshift allows the construction of a sample with close to uniform completeness over the majority of the DES Year 1 footprint. The true redshift distributions[7] ($n(z)$s henceforth) of the REDMAGIC galaxies are shown as the red solid lines in Fig. 1. These are histograms of the true redshift (z_{true}) for all galaxies within a given bin.

The $n(z)$s can also be estimated using, z_{RM}, and the associated uncertainty, $\sigma(z_{\mathrm{RM}})$, which is also provided by the REDMAGIC algorithm. These quantities are designed such that the probability of a

---

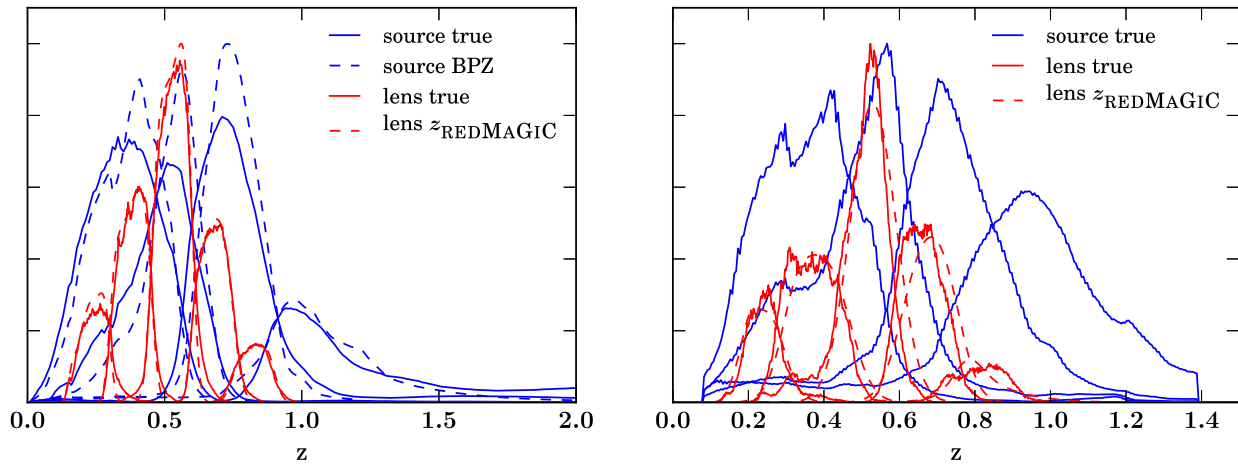[7]The comoving galaxy number density as a function of redshift.

Figure 1. Redshift distributions for the galaxy samples used. Red and blue indicate the REDMAGIC (*lens*) galaxies and the weak lensing source galaxies, respectively. Solid and dashed lines indicate the true distributions and those estimated from photometric redshifts, respectively. Left-hand panel: BCC, right-hand panel: MICE. As discussed in Section 4.2, we do not have BPZ photo-z estimates for the weak lensing source sample in MICE and by construction the true source redshift distributions match the BPZ estimates for the real data, apart from above $z = 1.4$, the maximum redshift of the MICE galaxies. For visual clarity, the lens and source redshift distributions have arbitrary normalization.

REDMAGIC galaxy having true redshift z_{true}, $p(z_{\text{true}}|z_{\text{RM}})$ is well approximated by a Gaussian distribution with mean and σ given by z_{RM} and $\sigma(z_{\text{RM}})$, respectively. Thus, the redshift distribution of each REDMAGIC tomographic bin can be estimated by stacking this Gaussian $p(z_{\text{true}}|z_{\text{RM}})$ estimate over all objects in that bin. This is how the REDMAGIC $n(z)$s are estimated on the real data, where true redshifts are not available, and is shown as the dashed red lines in Fig. 1.

For BCC, the visual agreement is good although there are some differences, for example the $n(z)$ looks to be underestimated at the high-redshift end of the first three redshift bins. For MICE, the REDMAGIC photo-z estimate also performs well, although some bias is apparent for the highest three redshift bins. Averaged over all simulations, there are 580 000 galaxies in our lens sample in BCC, compared with 660 000 in the DES Y1 data. Accounting for the difference in the areas of the footprints, these numbers agree to 5 per cent accuracy. This result also holds for the MICE lens sample, which contains 590 000 galaxies.

4.2 Weak lensing source sample

Unlike galaxy clustering measurements, for shear correlation function measurements, a galaxy sample whose completeness varies across the sky can be used, since number density fluctuations are not the quantity of interest. Instead, we require the sample to provide an unbiased estimate of the shear in any region of the sky. As in Section 2, we call this sample the source sample. We note that fluctuations in the galaxy number density can produce higher order effects on weak lensing statistics (see e.g. Hamana et al. 2002; Schmidt et al. 2009), but are below the few per cent level for the angular scales used here (MacCrann et al. 2017). For the real DES Y1 data, the weak lensing source selection depends on the outputs of 5+ parameter model-fitting shear estimation codes. To simulate this selection would require propagating our mock galaxy catalogues into image simulations with realistic galaxy appearances, which is beyond the scope of this work.

For the BCC, we perform cuts on galaxies' signal-to-noise and size relative to the point-spread-function (PSF) (assuming the spatial noise and PSF size distributions observed in the DES Y1 data) that

yield a sample with similar number density as the weak lensing sample in the real data. Specifically, we make the following cuts:

(i) Mask all regions of the footprint where limiting magnitudes and PSF sizes cannot be estimated.

(ii) $m_r < -2.5\log_{10}(1.5) + m_{r,\,\text{lim}}$

(iii) $\sqrt{r_{gal}^2 + (0.13 r_{\text{PSF}})^2} > 1.25 r_{\text{PSF}}$

(iv) $m_r < 22.01 + 1.217z$

where $m_{r,\,\text{lim}}$ and r_{PSF} are the limiting magnitude and PSF FWHM estimated from the data at the position of each galaxy. The first two cuts approximate signal-to-noise-related cuts that are be applied to shape catalogues in the data. Using only these, the BCC simulations yield number densities that exceed those found in the data, so also apply the third cut in order to more closely match the DES Y1 shape noise.

We then use the provided BPZ (Benítez 2000) photometric redshift estimates (BPZ is the fiducial method used to estimate photometric redshifts of the source galaxies in the real DES Y1 data, see Hoyle et al. 2017) to split the source sample into redshift bins. As in DES Collaboration et al. (2017), we split the weak lensing sample into four redshift bins, based on the mean of the BPZ redshift PDF, z_{mean}. Given that the size of the photometric redshift uncertainties is comparable to the bin widths, there is little to be gained by using more redshift bins. The four redshift bins are defined $0.2 < z_{\text{mean}} < 0.43$, $0.43 < z_{\text{mean}} < 0.63$, $0.63 < z_{\text{mean}} < 0.9$, $0.9 < z_{\text{mean}} < 1.3$. The $n(z)$s of the source sample are shown as the blue lines in Fig. 1. The histograms of true redshift for each bin are shown as solid lines, and $n(z)$s estimated using the BPZ redshift PDF estimates are shown as dashed lines. Again, some mis-estimation of the true $n(z)$s is apparent; we assess the impact of this in Section 5.4.

We do not have photometric redshift estimates for the MICE catalogs; so, instead randomly sample MICE galaxies to produce the same tomographic $n(z)$s as estimated by BPZ on the real data. In detail, we take the BPZ $n(z)$ estimates for the source sample from Hoyle et al. (2017), and for objects at a given true redshift in the MICE catalogs, we randomly assign a redshift bin with probability given by the relative amplitude of each tomographic $n(z)$ at that redshift. We additionally assign the MICE galaxies weights so that the weighted $n(z)$ for each tomographic bin matches the shape of

the BPZ $n(z)$ (within the redshift range of the MICE galaxies, which does not extend above $z = 1.4$). The resulting $n(z)$s are shown in the right-hand panel of Fig. 1.

We add Gaussian-distributed shape noise to the MICE source sample galaxies such that σ_e^2/n_{eff}, (where σ_e is the ellipticity dispersion, and n_{eff} is the effective galaxy number per unit area) matches the DES Y1 data. This ensures the covariance of the lensing statistics have the same shape noise contribution as the real DES Y1 data. Averaged over all BCC simulations, there are 23 million galaxies, compared to 26 million in the Y1 data. Taking into account the differences in area, these agree to 5.5 per cent accuracy.

5 RESULTS

In this section, we present measurements of the two-point correlation functions described in Section 2 on the galaxy samples described in Section 4. We then summarize the choices made for the analysis of these measurements, and finally present cosmological parameter constraints, and discuss how these should be interpreted.

5.1 Measurements and covariance

We estimate the two-point correlation functions using TREECORR[8] (Jarvis, Bernstein & Jain 2004). We compute correlation functions for all redshift bin combinations, i.e. 15 combinations for $w(\theta)$, 20 combinations for $\gamma_t(\theta)$, and 10 combinations for $\xi_\pm(\theta)$. We compute the correlation functions in 20 log-spaced angular bins in the angular range $2.5 < \theta < 250$ arcmin.

We show in the Appendix all the two-point correlation function measurements used. Figs A1–A4 show the two-point measurements on the BCC sims. Figs A5–A8 are the corresponding plots for the MICE-Y1 catalogs. Shaded regions indicated angular scales not used in the fiducial cosmological analysis because of theoretical uncertainties in the non-linear regime.

For all individual two-point functions and their combinations, we use the covariance matrix presented in Krause et al. (2017), which uses an analytic treatment of the non-Gaussian terms (Eifler et al. 2014; Krause & Eifler 2017) based on the halo model (Peacock & Smith 2000; Seljak 2000). We calculate the covariance assuming the true cosmology for each simulation. This is clearly not possible in an analysis of real data, where using an incorrect assumed cosmology (or, in fact not including the parameter dependence of the covariance matrix) could potentially introduce parameter biases. However, DES Collaboration et al. (2017) did demonstrate there was negligible change in the parameter constraints when using two different cosmologies to calculate the covariance matrix, so we do not believe our conclusions are very sensitive to this choice.

In the covariance calculation, we do not include the survey geometry corrections to the pure shape or shot noise covariance terms discussed in Troxel et al. (2018). For the DES Y1 geometry, the correction to the pure shot and shape noise contributions to the covariance are at most ~20 per cent, and this is at the largest scales, where shot/shape noise is generally subdominant.

We also do not include redshift bin cross correlations in $w(\theta)$, since we do not expect the fiducial theoretical model used, which assumes the Limber approximation and does not include redshift space distortions or magnification contributions, to be sufficiently accurate for these parts of the data vector (see e.g. LoVerde & Afshordi 2008, Montanari & Durrer 2015 for the importance of

[8]https://github.com/rmjarvis/TreeCorr

not using the Limber approximation, and including magnification, respectively for widely separated redshift bins).

5.2 Analysis choices

We summarize below our analysis choices, which closely follow those of Krause et al. (2017) and DES Collaboration et al. (2017), where the methodology and the application to data of the DES Y1 key cosmological analysis are described.

(i) **Gaussian Likelihood**. We assume the measured datavectors are multivariate-Gaussian distributed, with the covariance matrix described in Section 5.1. We note this is an approximation (see e.g. Sellentin & Heavens 2018); but any impact on parameter constraints will be mitigated by the significant contributions of shot noise and shape noise to the covariance matrix.

(ii) **Minimum angular scales.** For $w(\theta)$ and $\gamma_t(\theta)$, we use minimum angular scales corresponding to $8\,h^{-1}$ Mpc and $12\,h^{-1}$ Mpc at the mean redshift of the lens redshift bin, respectively (following DES Collaboration et al. 2017; Krause et al. 2017). These minimum scales are justified in Krause et al. (2017), who studied the potential impact of ignoring non-linear galaxy bias on the inferred cosmological parameters. This was estimated by generating fake DES Y1-like datavectors which included analytic models for non-linear galaxy bias, which were used as input to a cosmological parameter estimation pipeline that assumed linear bias. The minimum scales were chosen such that biases in cosmological parameters were small compared to the uncertainties on those parameters. The analysis of galaxy simulations in this work provides a further test of the effectiveness of these scale cuts.

For $\xi_\pm$, we use the same minimum angular scales as Troxel et al. (2017) and DES Collaboration et al. (2017), where we use the following procedure: for each redshift bin combination, we calculate the fractional difference in the expected signal when the matter power spectrum prediction used is modulated using templates from the OWLS simulations (Schaye et al. 2010). Separately for ξ_+ and ξ_- and for each redshift bin combination, we cut all angular scales smaller than and including the largest angular scale where the fractional difference exceeds 2 per cent. While this scale cut was motivated in Troxel et al. (2017) by the possibility of systematic biases due to baryonic physics not included in the simulations used here, we use it since removing these small scales will reduce the impact of finite simulation resolution on the cosmic shear signal.

(iii) **Galaxy bias model** As in the real data analysis (DES Collaboration et al. 2017), we marginalize over a single linear bias parameter, b_1^i per lens redshift bin i. We assume no redshift evolution of the bias across each redshift bin, but have verified that assuming passive evolution within a redshift bin i.e. $b^i(z) \propto D(z)$, where $D(z)$ is the linear growth factor, produces negligible differences in our parameter constraints.

(iv) **Redshifts.** For the results in Section 5.3 we use true redshifts to construct the $n(z)$s for the theory predictions. As discussed in Section 5.4, we find indications that the performance of BPZ on the BCC simulations is significantly worse than on the real data. Therefore, while we still use BPZ point redshift estimates to place galaxies in tomographic bins throughout, in Section 5.3 we show constraints which use true redshift information to construct the $n(z)$ (which enters the projection kernels $f_\alpha(\chi)$ in equation 6).

(v) **Matter power spectrum.** Following DES Collaboration et al. (2017), we use CAMB to calculate the linear matter power spectrum and HALOFIT (Smith et al. 2003; Takahashi et al. 2012) to model the nonlinear matter power spectrum.

(vi) **Limber approximation.** We use the Limber approximation to calculate all angular power spectra and do not include the contributions from redshift-space distortions; Krause et al. (2017) demonstrate that this is sufficiently accurate for DES Y1.

(vii) **Free parameters.** As well as five linear galaxy bias parameters, b_1^i, we marginalize over the same set of cosmological parameters (and use the same priors) as in DES Collaboration et al. (2017), with the exception of the sum of neutrino masses, $\sum m_\nu$. Since $\sum m_\nu = 0$ in both simulations suites, using a prior of $\sum m_\nu > 0$, would inevitably bias the inferred $\sum m_\nu = 0$ high, and given it is degenerate with other cosmological parameters, this would bias the inference of the other cosmological parameters. We also do not include nuisance parameters designed to account for effects not present in the simulations (so unlike the DES Collaboration et al. 2017, we do not maginalize over intrinsic alignment parameters or shear calibration uncertainties).

5.3 Fiducial cosmological parameter constraints

Having made measurements from all simulation realizations, and defined a modelling framework to apply to them, it is worth taking a step back to think about what information we wish to extract. Our aim is to estimate systematic biases in inferred parameters due to failures in our analysis and modelling of the simulations. We note that of course we will only be sensitive to those sources of systematic biases that are present in the simulations. For example, neither simulation suite here includes galaxy intrinsic alignments (and we do not include this effect in our modelling). Furthermore, as noted in Section 5.2, we remove the effect of photometric redshift biases for the results shown in this section, and use true redshift information (we discuss the photometric redshift performance for the BCC simulations in Section 5.4).

We estimate the size of systematic biases in our inferred parameters in the following way. We assume $P^{\rm sys}(\boldsymbol{\theta}, s_i)$, the potentially systematically biased posterior on parameters $\boldsymbol{\theta}$ we infer from a simulated datavector s_i is related to the true posterior by some constant translation in parameter space:

$$P^{\rm sys}(\boldsymbol{\theta}, s_i) = P(\boldsymbol{\theta} - \Delta\boldsymbol{\theta}|s_i). \tag{13}$$

We wish to estimate the posterior on $\Delta\boldsymbol{\theta}$. We start by considering $P(s_i|\boldsymbol{\theta}, \Delta\boldsymbol{\theta})$, the probability of drawing simulated datavector s_i given a value of $\Delta\boldsymbol{\theta}$, and a set of true parameters (i.e. those input to the simulation), $\boldsymbol{\theta}_{\rm true}$. This probability is independent of $\Delta\boldsymbol{\theta}$ such that

$$P(s_i|\boldsymbol{\theta}_{\rm true}, \Delta\boldsymbol{\theta}) = P(s_i|\boldsymbol{\theta}_{\rm true}) \tag{14}$$

$$= \frac{P(\boldsymbol{\theta}_{\rm true}|s_i)P(s_i)}{P(\boldsymbol{\theta}_{\rm true})} \tag{15}$$

$$= \frac{P^{\rm sys}(\boldsymbol{\theta}_{\rm true} + \Delta\boldsymbol{\theta}, s_i)P(s_i)}{P(\boldsymbol{\theta}_{\rm true})} \tag{16}$$

where in the second line we have used Bayes' theorem, and we have substituted equation (13) in the third line. We can again use Bayes' theorem to rewrite the left-hand side:

$$P(\Delta\boldsymbol{\theta}|s_i, \boldsymbol{\theta}_{\rm true}) = \frac{P(s_i|\boldsymbol{\theta}_{\rm true}, \Delta\boldsymbol{\theta})P(\Delta\boldsymbol{\theta})}{P(s_i)}. \tag{17}$$

Substituting equation (16), and assuming a flat prior $P(\Delta\boldsymbol{\theta})$, we have

$$P(\Delta\boldsymbol{\theta}|s_i, \boldsymbol{\theta}_{\rm true}) \propto P^{\rm sys}(\boldsymbol{\theta}_{\rm true} + \Delta\boldsymbol{\theta}, s_i). \tag{18}$$

This result makes sense intuitively – our potentially biased inferred posterior $P^{\rm sys}(\boldsymbol{\theta}, s_i)$ can be interpreted as the probability that the systematic bias $\Delta\boldsymbol{\theta}$ is equal to $\boldsymbol{\theta} - \boldsymbol{\theta}_{\rm true}$. Thus, if we find $P^{\rm sys}(\boldsymbol{\theta}, s_i)$ is consistent with $\boldsymbol{\theta} = \boldsymbol{\theta}_{\rm true}$, this implies $\Delta\boldsymbol{\theta}$ is consistent with zero.

Assuming our N simulated realizations are independent,[9] it follows that

$$P(\{s_i\}|\boldsymbol{\theta}_{\rm true}, \Delta\boldsymbol{\theta}) = \prod_{i=1}^{N} P(s_i|\boldsymbol{\theta}_{\rm true}, \Delta\boldsymbol{\theta}), \tag{19}$$

and

$$P(\Delta\boldsymbol{\theta}|\{s_i\}, \boldsymbol{\theta}_{\rm true}) \propto \prod_{i=1}^{N} P^{\rm sys}(\boldsymbol{\theta}_{\rm true} + \Delta\boldsymbol{\theta}, s_i). \tag{20}$$

In summary, we can estimate the systematic bias in our inferred parameters by computing the (potentially biased) parameter posterior $P^{\rm sys}(\boldsymbol{\theta}, s_i)$ from each simulation realization, and taking their product.

In this section, we focus on studying biases in $\Omega_{\rm m}$ and σ_8, the only two cosmological parameters well-constrained by DES Y1 data in DES Collaboration et al. (2017). The top panels of Fig. 2 shows constraints on $\Omega_{\rm m}$ and σ_8 from the BCC (*top-left*) and MICE (*top-right*) simulation suites, using all three two-point functions ($\xi_\pm(\theta)$, $\gamma_t(\theta)$, and $w(\theta)$). The dark orchid contours are the combined constraints from all realizations, calculated from the single-realization posteriors (shown in grey), using equation (20). Here and in all other plots, the contours indicate the 68 per cent and 95 per cent confidence regions.

For both MICE and BCC, the true cosmology (indicated by the black dashed lines) is within the 95 per cent contour, so we find no strong evidence for a non-zero $\Delta\boldsymbol{\theta}$. In the middle panels, we show the marginalized posteriors for the well-constrained parameter combination $S_8 = \sigma_8(\Omega_{\rm m}/0.3)^{0.5}$; again, the true value of S_8 is within the 95 per cent confidence region (indicated by the lighter shaded region under the posterior curve). Finally, the lower panels show the marginalized posteriors for $\Omega_{\rm m}$, which again are fully consistent with the true value for both BCC and MICE.

For comparison, in all panels we also indicate with green dashed lines the uncertainty on the parameters recovered from the real DES Y1 data in DES Collaboration et al. (2017), as 68 per cent and 95 per cent marginalised contours in the top row, and marginalized 1σ uncertainties in the middle and bottom rows. These uncertainties include marginalization over nuisance parameters, including those accounting for shear calibration uncertainty and intrinsic alignments, which were not considered in the analysis of the simulations in this work.

Fig. 3 meanwhile shows the constraints in the $\Omega_{\rm m} - \sigma_8$ plane for subsets of the datavector for the BCC (*left-hand panel*) and MICE simulations (*right-hand panel*). Again, these contours represent the combination of the posteriors from all individual simulation realizations. In both panels, the constraints from cosmic-shear only are

---

[9]We note that for neither of the simulation suites used here is this really true. For BCC, each set of 6 DES Y1 realizations is sourced from the same set of three N-body simulations, while for MICE, the two realizations are sourced from the same N-body simulation. While we ensure our Y1 realizations are extracted from non-overlapping regions, there will still be large-scale correlations between them. For our application, ignoring this is conservative, since unaccounted-for correlations between the realizations would tend to lead to fluctuations in the inferred parameters from their true values that are correlated between realizations, leading to over-estimates of systematic biases.
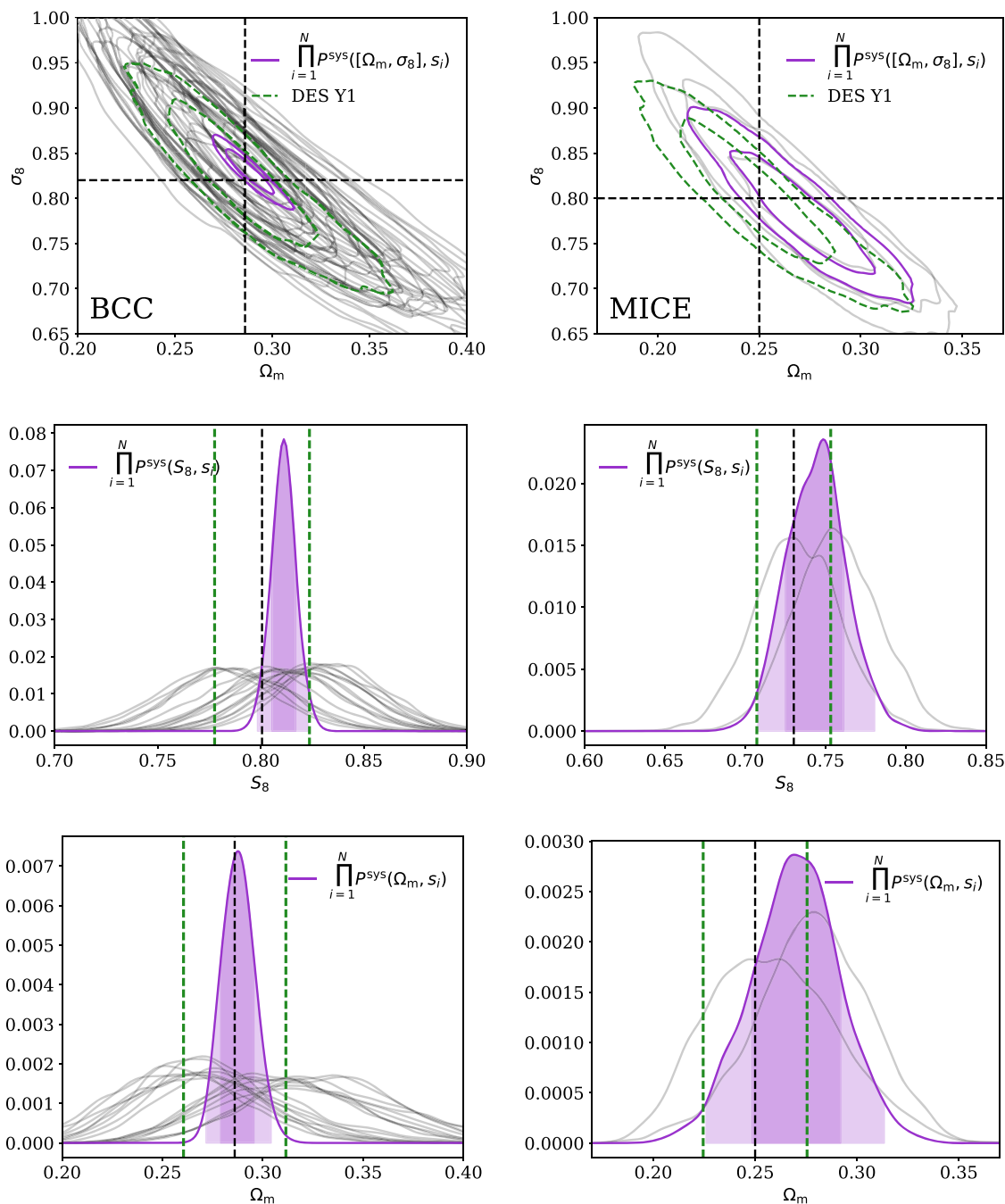
Figure 2. Cosmological constraints from all three two-point functions for the BCC (*left-hand panels*, 18 realizations) and MICE (*right-hand panels*, two realizations) simulation suites. The top panels show constraints on the present-day matter density, Ω_m and the clustering amplitude, σ_8. Contours contain 68 per cent and 95 per cent of the posterior probability. Grey contours show constraints from individual simulation realizations, while purple contours show the combination of these posteriors (see equation 20). The middle and bottom panels show the marginalized constraints on $S_8 = \sigma_8 \times (\Omega_m/0.3)^{0.5}$, and Ω_m, respectively. In all panels, the true parameter values (i.e. those input to the simulations) are indicated by the black dashed lines. In the top panels, the green dashed lines indicate the 68 per cent and 95 per cent confidence regions recovered from the real DES Y1 data in DES Collaboration et al. (2017), shifted to be centred on the input cosmology to the simulations. In the middle and lower-panels, the green dashed lines indicate the size of the $1 - \sigma$ uncertainty from DES Collaboration et al. (2017).

shown as the green dashed unfilled contours (labelled '$\xi_{\pm}$'), those from galaxy–galaxy lensing and galaxy clustering are shown as solid orange unfilled contours (labelled '$w + \gamma_t$'), and those from all three two-point functions are shown as filled dark-orchid contours (labelled '$\xi_{\pm} + w + \gamma_t$', these are the same as those in the upper

panels of Fig. 2). For both BCC and MICE, we see good agreement between the datavector subsets, and no evidence for disagreement with the true cosmology.

We can use these parameter constraints to make estimates of the biases in inferred parameters produced by systematic biases in
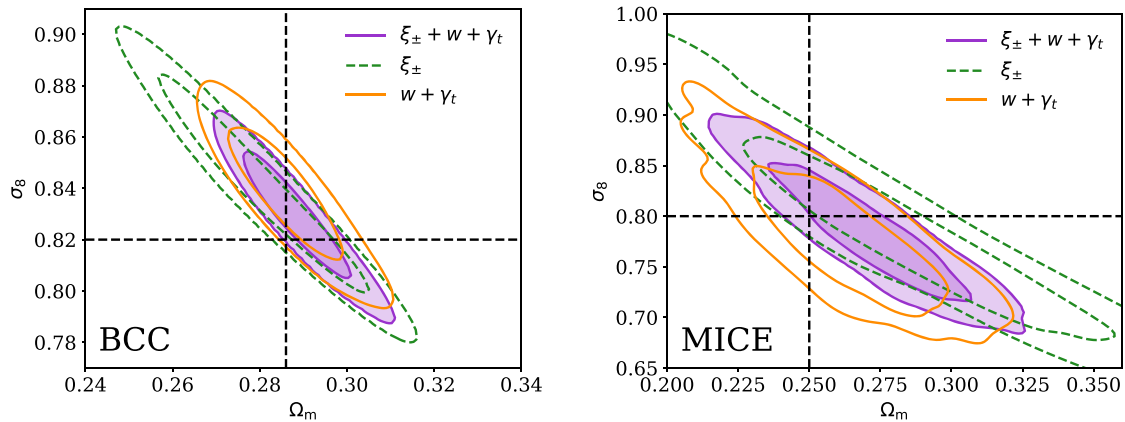
Figure 3. Constraints on the present day-matter density, Ω_m and the clustering amplitude, σ_8 from all three two-point functions (filled purple contours, labeled '$\xi_\pm + \gamma_t + w$'), cosmic shear-only (dashed green contours, labeled '$\xi_\pm$'), and galaxy-galaxy lensing and clustering (solid-lined orange contours, labeled '$\gamma_t + w$'), for the BCC simulations (left-hand panel) and MICE simulations (right-hand panel). We show combined constraints from all simulation realizations. The intersection of the black dashed lines indicates the true parameter values (i.e. those input to the simulations).

the parameter inference (assuming perfect simulations). Note that these estimates are conditional on the specific set of simulated data that were realized, $\{s_i\}$. Clearly, it is desirable to have systematic biases be sub-dominant to statistical uncertainties. Therefore, for constraints from all three two-point functions, we report the probability that the bias in the inferred parameter θ (where θ is Ω_m or S_8) are within $\sigma_{Y1}(\theta)$ of their true values, where $\sigma_{Y1}(\theta)$ is the 1σ uncertainty on parameter θ recovered by DES Collaboration et al. (2017). We denote this quantity $P(\Delta\theta < \sigma_{Y1})$. DES Collaboration et al. (2017) find $\sigma_{Y1}(S_8) = 0.023$ and $\sigma_{Y1}(\Omega_m) = 0.026$ (for convenience, we use half the difference between the reported upper and lower 68 per cent confidence limits rather than propagating asymmetric errorbars). Of course, this should not be interpreted as an estimate of the impact of *all* systematic errors, only those tested by the simulations. With this caveat duly noted, $P(\Delta\theta < \sigma_{Y1})$ can be calculated as the integral of the posteriors in the middle and lower panels of Fig. 2 between the dashed lines, for $\theta = S_8$ and Ω_m, respectively. Ideally, one could also calculate e.g. $P\left(\Delta\theta < \frac{1}{2}\sigma_{Y1}\right)$, however, given our available simulation volume, we do have sufficient statistical power to meaningfully constrain parameter biases to this precision.

For the BCC simulations, we find $P(\Delta S_8 < \sigma_{Y1}) = 0.98$ and $P(\Delta\Omega_m < \sigma_{Y1}) = 1.00$ (we report these probabilities to two decimal places), indicating that we can be confident that systematic biases in our inference of S_8 and Ω_m from the BCC simulations are less than the DES Y1 1σ uncertainty for those parameters.

For the MICE simulations, we find $P(\Delta S_8 < \sigma_{Y1}) = 0.66$ and $P(\Delta\Omega_m < \sigma_{Y1}) = 0.57$. Again, more simulation volume is required to make strong statements about the sub-dominance (or not) of systematic errors to statistical errors from the MICE simulations. This does not make the analysis of the MICE simulations a pointless exercise; we can comfort ourselves with the fact that we could have uncovered large (i.e. larger than the DES Y1 1σ uncertainty) systematic biases, and did not.

Table 2 summarizes our parameter bias results for both simulation suites and all subsets of the datavector considered.

5.4 Photometric redshifts

Photometric redshift estimation is one of the major challenges for extracting precise cosmological information from imaging surveys

(e.g. Schmidt et al. 2014). In this section, we test the effects of photometric redshift biases on the inferred cosmological parameters for the BCC simulation suite. For the fiducial analyses of real DES Y1 data, BPZ was used to estimate the $n(z)$s of the source sample, as described in Hoyle et al. (2017). These $n(z)$ estimates were further refined by comparison to two independent photo-z methods, and shifts of the form $n^i(z) \rightarrow n^i(z + \delta z^i)$ were applied to each redshift bin i, with uncertainty in the δz^i marginalized over as part of the cosmological parameter estimation (with Gaussian priors of width [0.016, 0.013, 0.011, 0.022]).

We do not implement the two independent photo-z methods used to correct the BPZ $n(z)$s on these simulations (this would require significantly expanding the scope of the simulations), but as an idealised proxy, we do apply shifts δz^i to the BPZ $n(z)$ estimates such that they have the correct mean redshift (see case (iii) below).

For the BCC simulations (we do not use photo-z estimates for the source sample in MICE), we compare the recovered cosmological parameters in the following cases:

(i) We use the true redshifts to construct the $n(z)$s for both lenses and sources; this was our fiducial treatment in Section 5.3.

(ii) We use true redshifts to construct the $n(z)$ for the lenses, but BPZ estimates to construct the $n(z)$ for the sources. For this case, we marginalize over a shift δz^i for each source redshift bin i, with independent Gaussian priors with mean zero, and width 0.02 (this is same order as those used in DES Collaboration et al. 2017)

(iii) The same as case (ii), but we first shift the BPZ $n(z)$ estimates such that they have the correct mean redshift.

(iv) The same as case (ii), but we now also use photometric redshifts to construct the lens sample $n(z)$s.

Given the size of the DES Y1 area, there is very little variation in the $n(z)$s between simulated realizations, therefore we can assess the effect of using photometric redshift biases by comparing the cosmological constraints inferred from the mean datavector across all realizations when we use the true redshifts to construct the theoretical prediction for the datavector, to when we use photometric redshift estimates in the theoretical prediction. We use a covariance matrix appropriate for a single DES Y1 realization in the likelihood calculation, which naturally puts any differences in the contours in the context of DES Y1 uncertainties.

Table 2. A summary of constraints on parameter biases inferred from both simulation suites. The $\Delta\Omega_m$ and ΔS_8 provide the absolute bias in Ω_m and S_8 (and 68% confidence intervals) with respect to the truth input to the simulations. For comparison, the uncertainty on these parameters for the accompanying analysis in DES Collaboration et al. (2017) is 0.026 and 0.023 respectively; statistically significant biases of this level would be a cause for concern.

Dataset	$\Delta\Omega_m$	$P(\Delta\Omega_m < \sigma_{Y1})$	ΔS_8	$P(\Delta S_8 < \sigma_{Y1})$
BCC $\xi_\pm + w + \gamma_t$	0.0017 ± 0.0084	1.00	0.0106 ± 0.0058	0.97
BCC $\xi_\pm$	-0.0125 ± 0.0120	0.84	0.0067 ± 0.0059	0.99
BCC $w + \gamma_t$	-0.0010 ± 0.0085	1.00	0.0156 ± 0.0077	0.81
MICE $\xi_\pm + w + \gamma_t$	0.0191 ± 0.0217	0.57	0.0183 ± 0.0182	0.67
MICE $\xi_\pm$	0.0198 ± 0.0434	0.39	0.0239 ± 0.0213	0.49
MICE $w + \gamma_t$	0.0052 ± 0.0226	0.68	-0.0024 ± 0.0262	0.61
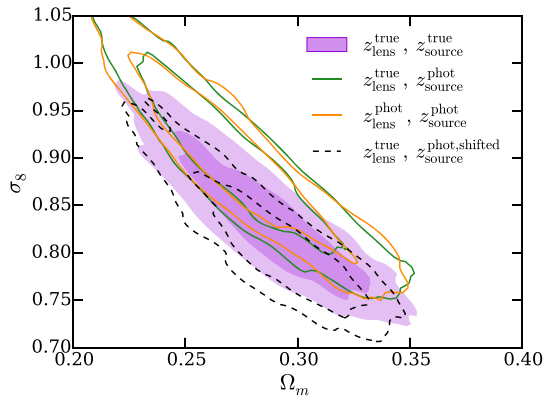
Figure 4. The impact of using photometric redshift estimates. For all contours, the datavector is the mean of all BCC realisations. Purple filled contours use the true redshift distributions for both lens and source galaxies. Note in this case galaxies are binned according to their photo-z, but the $n(z)$ for each redshift bin is estimated using true redshifts. The green unfilled contours use source redshift distributions estimated using BPZ photo-zs, while the orange unfilled contours additionally use the photometric redshift estimates from the the REDMAGIC algorithm, z_{RM} for the lenses. The black dashed contours use BPZ to estimate the source $n(z)$s, shifted in redshift to have the correct mean (see Section 5.4 for details).

Fig. 4 demonstrates that the inferred cosmological parameters do change significantly when using photometric redshifts in the BCC simulations. The green contour illustrates case (ii); in this case, S_8 is significantly biased with respect to the fiducial result (the filled purple contour) by 0.038, greater than the achieved 1σ uncertainty for DES Y1. The dashed black contour shows case (iii), where the BPZ $n(z)$ estimates are first shifted to have the correct mean. The result is improved, but the bias in S_8 of 0.020 with respect to the fiducial case is still non-negligible. Using photometric redshifts for the lens $n(z)$s does not introduce significant parameter bias - the S_8 bias for case (iv) differs from that for case (ii) by only 4×10^{-3}. This implies that the z_{RM} photo-zs in BCC are comfortably performing sufficiently well for DES Y1.

It appears then that marginalizing over δz_i for the source redshift bins with the above priors is an insufficiently flexible scheme to account for biases in the BPZ $n(z)$ estimates for the BCC simulations. On the real DES data, the opposite conclusion was reached in Hoyle et al. (2017), with BPZ performing sufficiently well in comparison to a re-weighted COSMOS sample with high-precision photo-zs (Laigle et al. 2016) and cross-correlation methods. Given this result, it is likely that BPZ is performing worse on the BCC simulations than the real DES data. This is demonstrated in Fig. 5,
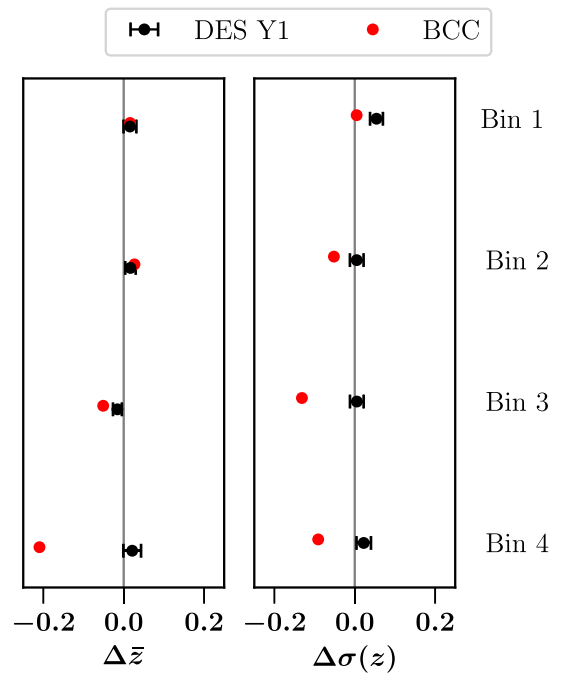
Figure 5. Estimates of the bias in the mean redshift ($\bar{z}$) and the bias in the redshift standard deviation ($\sigma(z)$) reported by BPZ for each source redshift bin. For the BCC simulations (red points) these biases can be computed exactly, while for the real DES Y1 data (black points), these are estimated from comparison with a re-weighted COSMOS sample with high-precision redshift information (Hoyle et al. 2017). For the two highest source redshift bins, we see much larger biases in both the mean redshift and the redshift standard deviation for BCC than we do for the DES Y1 data. While biases in $\bar{z}$ can be accounted for using the δz^i parameterization described in Section 5.4, biases in $\sigma(z)$ are not accounted for by this parameterization.

where we show estimates of the bias in the mean redshift ($\bar{z}$) and the bias in the width (the standard deviation, $\sigma(z)$) of each source redshift bin. For the BCC $n(z)$'s, we can use true redshift information to calculate these quantities exactly, while for the DES Y1 data, these biases are estimated by comparison to the aforementioned COSMOS sample. For the DES Y1 points, error bars indicate the uncertainty of the COSMOS-based estimates of $\bar{z}$ and $\sigma(z)$, using the methodology of and including all effects discussed in Hoyle et al. (2017).

Particularly for the highest two redshift bins, for BCC we see large biases in both the mean redshift, and the width of the redshift distribution. While the impact of the former could be mitigated by the δz_i nuisance parameters, biases in the width of the $n(z)$s can not

be. This is the likely explanation for why marginalizing over δz_i did not mitigate BPZ redshift biases sufficiently for BCC.

The conclusion that the BPZ performance is worse on BCC than on the real DES data of course depends on the reliability of the COSMOS-based photo-z validation, especially for the highest-redshift bin where a clustering-based n(z) estimate was not available as additional validation. Several potential sources of biases in the n(z) estimation using the COSMOS photo-zs are investigated and quantified in Hoyle et al. (2017); these contribute to the error bars on the DES Y1 points in Fig. 5, which are still much smaller than the differences apparent between DES Y1 and BCC. As discussed in Hoyle et al. (2017), for the DES Y1 magnitude range ($\lesssim 23.5$), $n(z)$ biases due to errors in the COSMOS photo-zs of greater than a few per cent seem very unlikely based on the results of Laigle et al. (2016). We find it very unlikely therefore that biases at the level we see for BPZ on BCC (e.g. 20 per cent in mean redshift for the highest z bin) could be present for the BPZ and COSMOS estimates on the DES Y1 data.

Potential reasons for the poor performance of BPZ will be explored further in DeRose et al. (2018). Particularly at high redshift, there may be a mismatch between the BPZ templates and the galaxy colours simulated in the BCC since the BPZ templates include a redshift evolution correction based on higher redshift spectroscopic data (see Hoyle et al. 2017) that is not present in the low-redshift SDSS data used by ADDGALS (see Section 3.1.2). As discussed in Section 4.2, we note also that our procedure for selecting the source sample from the BCC was highly simplified compared to the procedure on the data. Even if the galaxy colours in the BCC matched the real Universe perfectly, this difference in selection could produce a source sample in BCC on which BPZ performs differently as compared to the real data.

We note here that generating mock galaxies with realistic joint distributions of clustering properties, colours, and redshift down to the magnitude limits, and in the redshift ranges required for DES, is extremely challenging. Iterative improvements in empirical and theoretical galaxy models with comparison to DES and other large photometric and spectroscopic datasets will likely be required to meet this challenge.

6 DISCUSSION

Combined weak lensing and clustering analyses on Stage III galaxy surveys are still in their infancy, but already present a significant step forward for cosmological inference from these surveys (van Uitert et al. 2017; DES Collaboration et al. 2017; Joudaki et al. 2018). Even in the absence of systematics, this multi-probe approach allows more cosmological information to be extracted, and when uncertain contributions from systematic effects are included, can greatly reduce the degradation in cosmological constraining power they cause. However, such analyses rely on various theoretical assumptions, and assume that observational and astrophysical systematics can be treated accurately, making validation of the methodology extremely important.

In this work, we have attempted to validate the methodology used on DES Y1 data by performing a similar analysis of tailored survey simulations. Simulations have of course been extensively used in cosmology analyses of photometric data sets. Related recent cosmology analyses include Mandelbaum et al. (2013), who performed a detailed study of the galaxy–matter cross-correlation in simulations to validate their theoretical modeling. van Uitert et al. (2017) presented a similar combined weak lensing and galaxy clustering analysis on KiDS data to that considered here and tested aspects

of their analysis on tailored simulations. However, these did not include a realistic lens sample to test the galaxy bias modeling. In this work, we go further than previous analyses in attempting to simulate both galaxy clustering and lensing observables (rather than quantities that are not directly observable such as the galaxy–matter correlation function), estimated from galaxy samples that are selected using the same or at least approximate versions of the galaxy selection process used on the real data. By using observable quantities, we ensure that higher-order effects like magnification and reduced shear are included, so we are implicitly testing the impact of ignoring these effects in our theoretical modelling.

These simulations contain many of the complexities of real data: spatially varying magnitude errors due to depth variations affect galaxy selection, the statistical connection between galaxies and matter is more complex than our simple theoretical models, and photometric redshift algorithms have been implemented (albeit further work on the galaxy colours is required to make this last aspect more informative). Table 3 summarizes complexities present in real data that are relevant to a galaxy clustering and weak lensing analysis, and indicates whether they are included in the simulations used in this work. For those that are included, our analysis of the simulations constitutes a validation of their treatment in our cosmological parameter estimation pipeline.

As indicated in Table 3, there are various potential systematic effects in real data that are not included in the simulations used here. For example, image simulations are likely required to test the accuracy of photometry and shear estimation pipelines (e.g. Bridle et al. 2009; Mandelbaum et al. 2014). In order to produce image simulations with realistic distributions of galaxy properties (including clustering), it will be desirable to propagate the type of simulation used in this work to the image level (rather than just the mock catalogues used here). Some progress on this has already been made by Chang et al. (2015).

We also note that neither simulation suite used here includes galaxy intrinsic alignments, which potentially contaminates the shear correlation functions and the galaxy–galaxy lensing signal. We believe including intrinsic alignments in future galaxy survey simulations should be prioritized, as it is one of the major systematics faced by weak lensing analyses (Troxel & Ishak 2015; Joachimi et al. 2015). Another primary systematic for cosmic shear analyses, the effect of baryonic physics on the matter power spectrum (see e.g. White 2004; Zhan & Knox 2004; Semboloni et al. 2011), is also not included here. These effects, often termed *astrophysical systematics*, clearly depend on additional physics to that implemented in the *N*-body simulations used here. Both of these effects are areas of active investigation using hydrodynamic simulations (e.g. Chisari et al. 2018, 2017).

The galaxy bias, especially on small scales, of course also depends on the simulation implementation. Here again, hydrodynamic simulations are arguably closer to a first-principles approach to simulating galaxies than the empirical relations used in BCC and MICE. However they have a much higher computational cost, and much of the relevant physics still occurs on scales below the resolution limit of any current simulations that are large enough in volume to be applicable to cosmological analyses. It is likely that iterative comparison of the galaxy survey data such as the Dark Energy Survey are providing, simulations which use empirical relations to add galaxies like the ones used here, and hydrodynamic simulations will be required to inform us of the true behavior of galaxy bias. Nonetheless, we have shown that reasonable models for how galaxies trace the density field, implemented in the BCC and MICE simulations, show no strong evidence of bias in cosmo-

Table 3. A list of phenomena relevant to the combined clustering and weak lensing analysis presented here that exist in real data. We indicate whether they are included in the simulations used in this work, and thus whether our treatment of the effect is tested by the analysis of the simulations presented here. 'Higher-order lensing effects' refers to contributions to the weak lensing shear at higher than first order in the gravitational potential (see e.g. Krause & Hirata 2010) that are captured by full ray-tracing as in the BCC. 'Beyond Limber angular statistics + RSD' refers to the deviation of the angular power spectra in the simulations from that predicted assuming the Limber approximation and ignoring redshift space distortions, as in our modelling. Although the BCC catalogues do provide photo-z estimates, the differences between the performance of BPZ on the simulated and real data limited their usefulness (see Section 5.4) – the '($\sqrt{}$)' symbol in the 'Photo-z bias' row reflects this.

Real-data complexity	Included in BCC	Included in MICE
Photometry and shear estimation biases	×	×
Higher-order lensing effects	√	×
Intrinisc alignments	×	×
Nonlinear galaxy bias	√	√
Beyond-Limber angular statistics + RSD	√	√
Magnification effect on number counts	√	√
Baryonic effects on the matter distribution	×	×
Photo-z biases	(√)	×
Spatially varying photometric noise	√	√
Non-Gaussian distributed datavectors	√	√

logical parameter inference, which should provide confidence in the robustness of the cosmological parameter constraints presented in the companion papers (DES Collaboration et al. 2017; Troxel et al. 2017).

Given the amount of simulation volume currently available for the MICE simulations, we are unable to make a very definitive statement about the size of systematic biases with relation to the DES Y1 parameter uncertainties. For the BCC simulations, on the other hand, we do find convincing evidence that inferred parameter biases are smaller than the DES Y1 1σ uncertainties. Updated versions of both simulation suites that will be used for upcoming DES cosmology analyses are already reasonably advanced in their development, and will provide larger simulation volumes, as well as implementing improved empirical relations between galaxy colours and clustering properties.

REFERENCES

Alam S. et al., 2017, MNRAS, 470, 2617
Albrecht A. et al., 2006, preprint (arXiv:e-print)
Bartelmann M., Schneider P., 2001, Phys. Rep., 340, 291
Becker M. R., 2013, MNRAS, 435, 115
Benítez N., 2000, ApJ, 536, 571
Betoule M. et al., 2014, A&A, 568, A22
Blanton M. R. et al., 2003, AJ, 125, 2348
Bridle S. et al., 2009, Ann. Appl. Stat., 3, 6
Carretero J., Castander F. J., Gaztañaga E., Crocce M., Fosalba P., 2015, MNRAS, 447, 646
Chang C. et al., 2015, ApJ, 801, 73
Chisari N. E. et al., 2017, MNRAS, 472, 1163
Chisari N. E. et al., 2018, preprint (arXiv:1801.08559)
Conroy C., Wechsler R. H., Kravtsov A. V., 2006, ApJ, 647, 201
Cooper M. C. et al., 2006, MNRAS, 370, 198
Crocce M., Pueblas S., Scoccimarro R., 2006, MNRAS, 373, 369
DeRose J., Wechsler R., Rykoff E. et al., 2018, preprint (arXiv:e-print)
DES Collaboration et al., 2017, Phys. Rev. D. reprint (arXiv:1708.01530)
Drlica-Wagner A. et al., 2017, submitted to Astrophys. J. Suppl. Ser.
Eifler T., Krause E., Schneider P., Honscheid K., 2014, MNRAS, 440, 1379
Elvin-Poole J. et al., 2017, Phys. Rev. D, preprint (arXiv:170801536)
Flaugher B. et al., 2015, AJ, 150, 1
Fosalba P., Gaztañaga E., Castander F. J., Crocce M., 2015a, MNRAS, 447, 1319
Fosalba P., Crocce M., Gaztañaga E., Castander F. J., 2015b, MNRAS, 448, 2987
Fry J. N., Gaztanaga E., 1993, ApJ, 413, 447
Górski K. M., Hivon E., Banday A. J., Wandelt B. D., Hansen F. K., Reinecke M., Bartlmann M., 2005, ApJ, 622, 759
Hamana T., Colombi S. T., Thion A., Devriendt J. E. G. T., Mellier Y., Bernardeau F., 2002, MNRAS, 330, 365
Heitmann K., White M., Wagner C., Habib S., Higdon D., 2010, ApJ, 715, 104
Hirata C. M. et al., 2004, MNRAS, 353, 529
Hoyle B. et al., 2017, MNRAS, 478, 592
Jarvis M., Bernstein G., Jain B., 2004, MNRAS, 352, 338
Joachimi B. et al., 2015, SSRv, 193, 1
Joudaki S. et al., 2018, MNRAS, 474, 4894
Kilbinger M., 2015, Rep. Prog. Phys., 78, 086901
Krause E., Eifler T., 2017, MNRAS, 470, 2100
Krause E., Hirata C. M., 2010, A&A, 523, A28
Krause E. et al., 2017, submitted to Phys. Rev. D, preprint (arXiv:1706.09359)
Kwan J., Heitmann K., Habib S., Padmanabhan N., Lawrence E., Finkel H., Frontiere N., Pope A., 2015, ApJ, 810, 35
Kwan J. et al., 2017, MNRAS, 464, 4045

Laigle C. et al., 2016, ApJS, 224, 24
Landy S. D., Szalay A. S., 1993, ApJ, 412, 64
Lehmann B. V., Mao Y.-Y., Becker M. R., Skillman S. W., Wechsler R. H., 2017, ApJ, 834, 37
Lewis A., 2004, Phys. Rev. D, 70, 043011
Limber D. N., 1953, ApJ, 117, 134
LoVerde M., Afshordi N., 2008, Phys. Rev. D, 78, 123506
LSST Dark Energy Science Collaboration, 2012, preprint (arXiv:1211.0310)
MacCrann N. et al., 2017, MNRAS, 465, 2567
Maddox S. J., Efstathiou G., Sutherland W. J., 1996, MNRAS, 283, 1227
Mandelbaum R., Slosar A., Baldauf T., Seljak U., Hirata C. M., Nakajima R., Reyes R., Smith R. E., 2013, MNRAS, 432, 1544
Mandelbaum R. et al., 2014, ApJS, 212, 5
Miyazaki S. et al., 2002, PASJ, 54, 833
Montanari F., Durrer R., 2015, J. Cosmol. Astropart. Phys., 10, 070
Peacock J. A., Smith R. E., 2000, MNRAS, 318, 1144
Perlmutter S. et al., 1999, ApJ, 517, 565
Planck Collaboration et al., 2015, AAP, 594, A13
Prat J. et al., 2017, Phys. Rev. D, preprint (arXiv:1708.01537)
Riess A. G. et al., 1998, AJ, 116, 1009
Ross A. J. et al., 2017, MNRAS, 464, 1168
Rozo E. et al., 2016, MNRAS, 461, 1431
Schaye J. et al., 2010, MNRAS, 402, 1536
Schaye J. et al., 2015, MNRAS, 446, 521
Schmidt F., Rozo E., Dodelson S., Hui L., Sheldon E., 2009, ApJ, 702, 593
Schmidt S. J., Newman J. A., Abate A. the Spectroscopic Needs White Paper Team, 2014, preprint (arXiv:1410.4506)
Seljak U., 2000, MNRAS, 318, 203
Sellentin E., Heavens A. F., 2018, MNRAS, 473, 2355
Semboloni E., Hoekstra H., Schaye J., van Daalen M. P., McCarthy I. G., 2011, MNRAS, 417, 2020
Singh S., Mandelbaum R., Seljak U., Slosar A., Vazquez Gonzalez J., 2017, MNRAS, 471, 3827
Sinha M., Berlind A. A., McBride C. K., Scoccimarro R., Piscionere J. A., Wibking B. D., 2017, preprint (arXiv:1708.04892)
Smith R. E. et al., 2003, MNRAS, 341, 1311
Springel V., 2005, MNRAS, 364, 1105
Stebbins A., 1996, preprint (arXiv:e-print)
Takahashi R., Sato M., Nishimichi T., Taruya A., Oguri M., 2012, ApJ, 761, 152
Troxel M. A., Ishak M., 2015, Phys. Rep., 558, 1
Troxel M. A. et al., 2017, Phys. Rev. D, preprint (arXiv:1708.01538)
Troxel M. A. et al., 2018, preprint (arXiv:1804.10663)
van Uitert E. et al., 2017, preprint (arXiv:1706.05004)
Vogelsberger M. et al., 2014, MNRAS, 444, 1518
Wechsler R., DeRose J., Busha M. et al., 2018, preprint (arXiv:e-print)
Weinberg D. H., Mortonson M. J., Eisenstein D. J., Hirata C., Riess A. G., Rozo E., 2013, Phys. Rep., 530, 87
White M., 2004, Astropart. Phys., 22, 211
Zehavi I. et al., 2005, ApJ, 630, 1
Zhan H., Knox L., 2004, ApJ, 616, L75

APPENDIX: TWO-POINT CORRELATION FUNCTION MEASUREMENTS

Figs A1–A4 show the two-point correlation function measurements from the BCC simulations. Figs A5–A8 show two-point correlation function measurements from the MICE simulations.
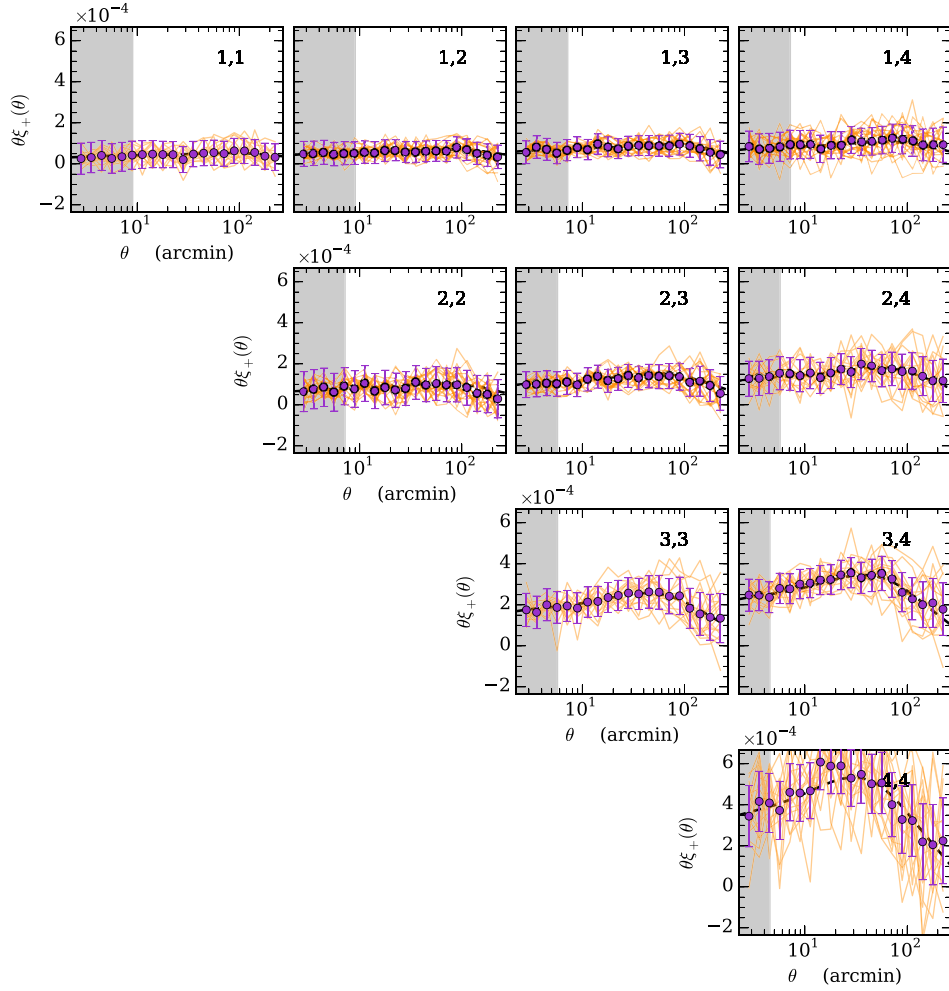
Figure A1. Measurement of $\xi_+(\theta)$ in the BCC simulations. Dark orchid data points are the mean across all 18 simulations, while orange lines indicate measurements from individual realizations. Errorbars indicate the expected uncertainty from a single DES Y1 realization. The line is the theoretical prediction assuming the true cosmology. Grey-shaded regions are excluded from the fiducial analysis.
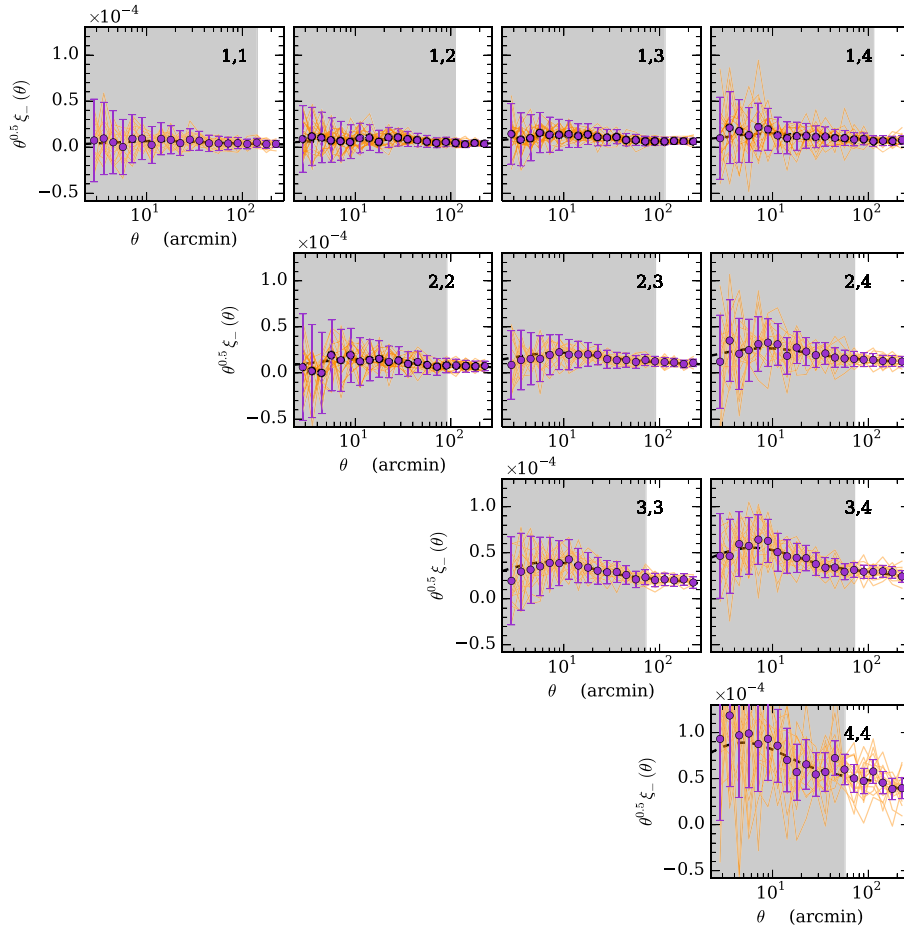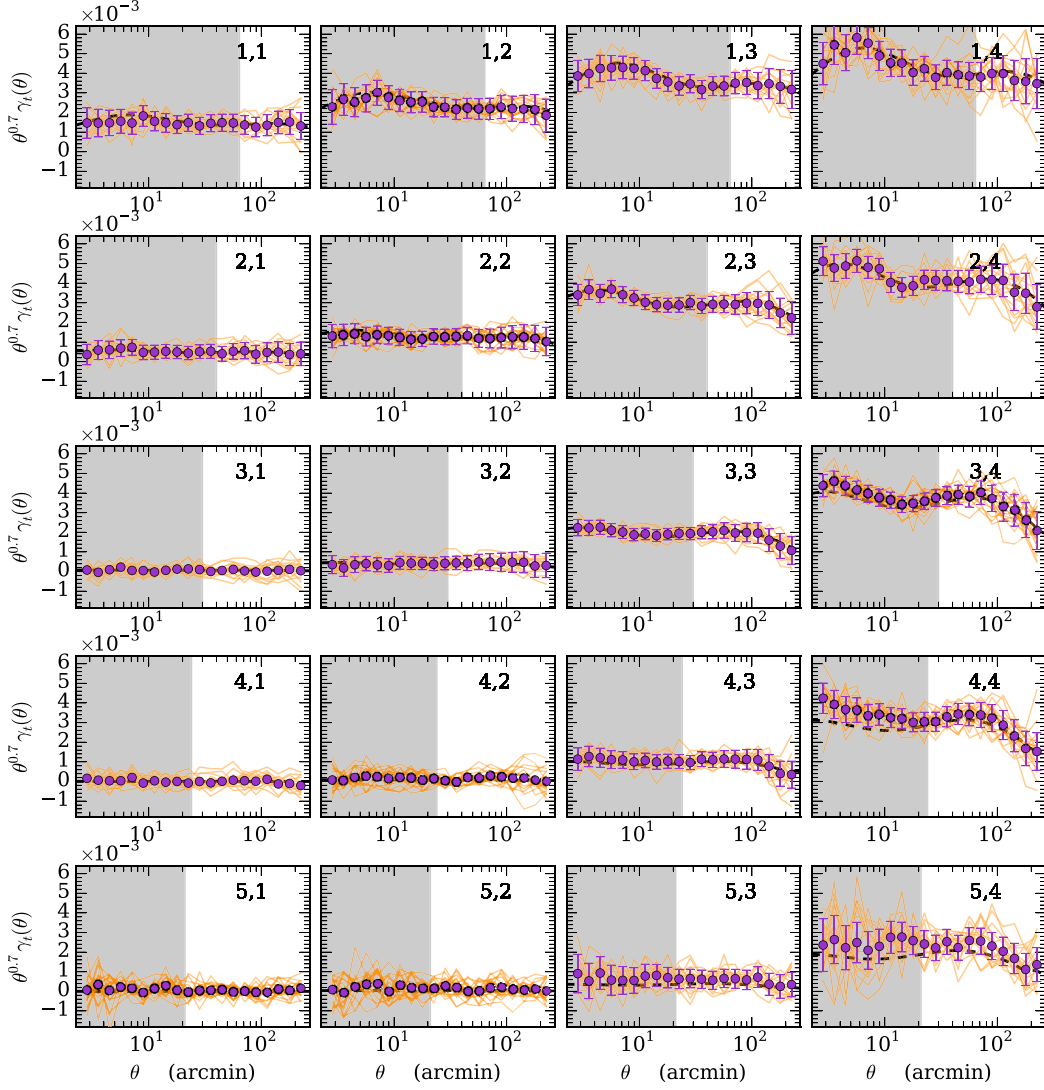
Figure A2. Measurement of $\xi_-(\theta)$ in the BCC simulations. Dark orchid data points are the mean across all 18 simulations, while orange lines indicate measurements from individual realizations. Errorbars indicate the expected uncertainty from a single DES Y1 realization. The line is the theoretical prediction assuming the true cosmology. Grey-shaded regions are excluded from the fiducial analysis.

Figure A3. Measurement of $\gamma_t(\theta)$ in the BCC simulations. Dark orchid data points are the mean across all 18 simulations, while orange lines indicate measurements from individual realizations. Errorbars indicate the expected uncertainty from a single DES Y1 realization. The line is the theoretical prediction assuming the true cosmology, with the best-fit galaxy bias from the mean of all realizations. Grey-shaded regions are excluded from the fiducial analysis.
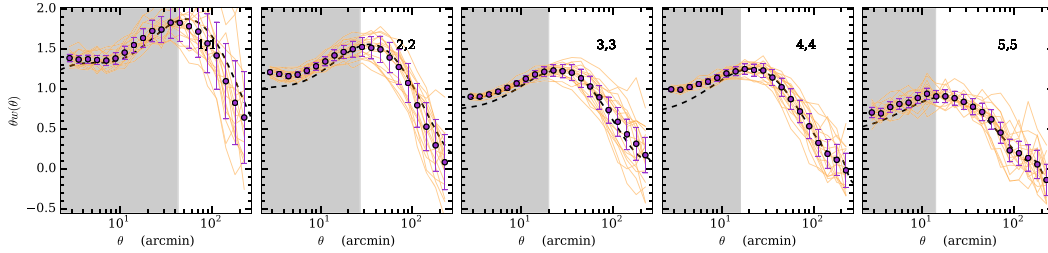

Figure A4. Measurement of $w(\theta)$ in the BCC simulations. Dark orchid data points are the mean across all 18 simulations, while orange lines indicate measurements from individual realizations. Errorbars indicate the expected uncertainty from a single DES Y1 realization. The line is the theoretical prediction assuming the true cosmology, with the best-fit galaxy bias from the mean of all realizations. Grey-shaded regions are excluded from the fiducial analysis.
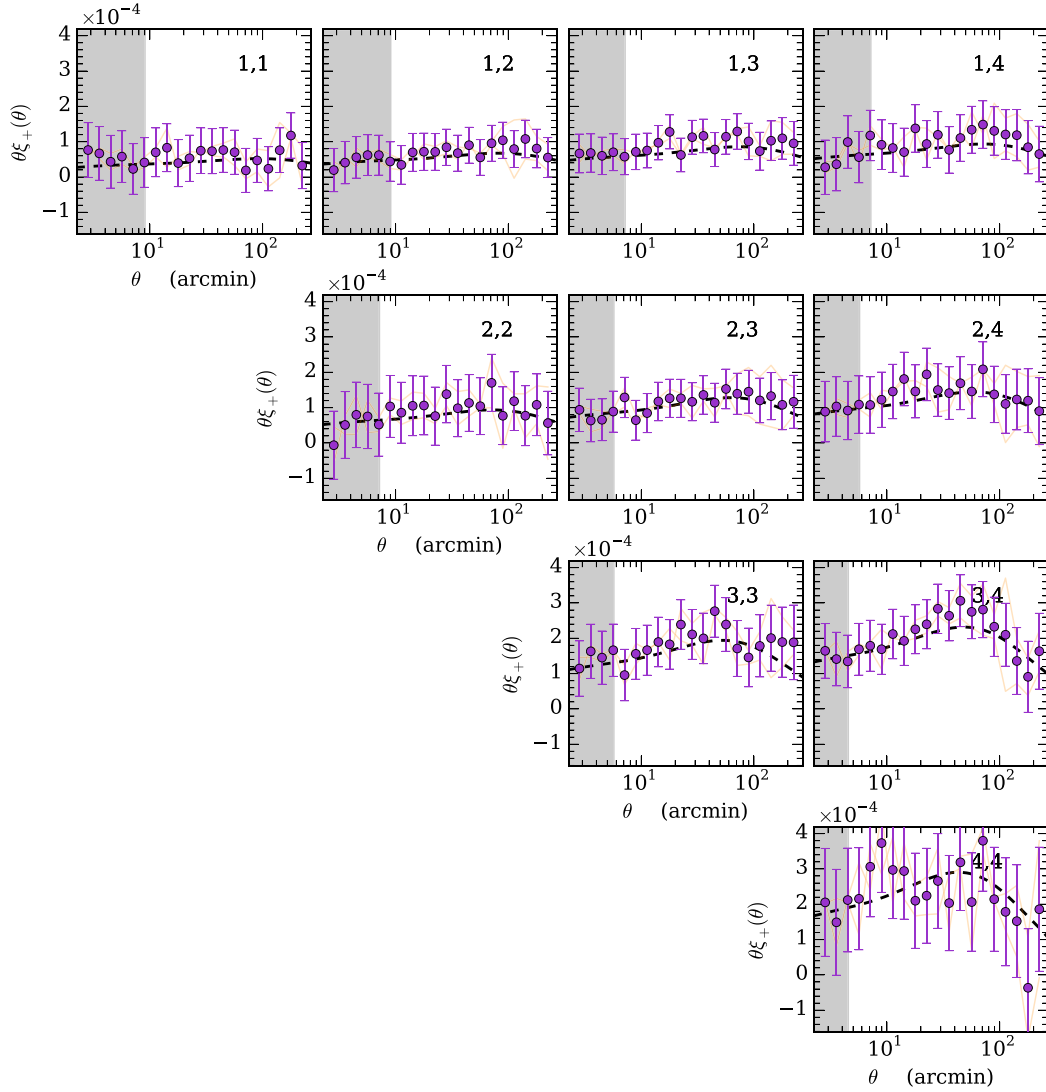
Figure A5. Measurement of $\xi_+(\theta)$ in the MICE simulations. Dark orchid data points are the mean across the two DES Y1 realizations, while orange lines indicate measurements from individual realizations. Errorbars indicate the expected uncertainty from a single DES Y1 realization. The line is the theoretical prediction assuming the true cosmology. Grey-shaded regions are excluded from the fiducial analysis.
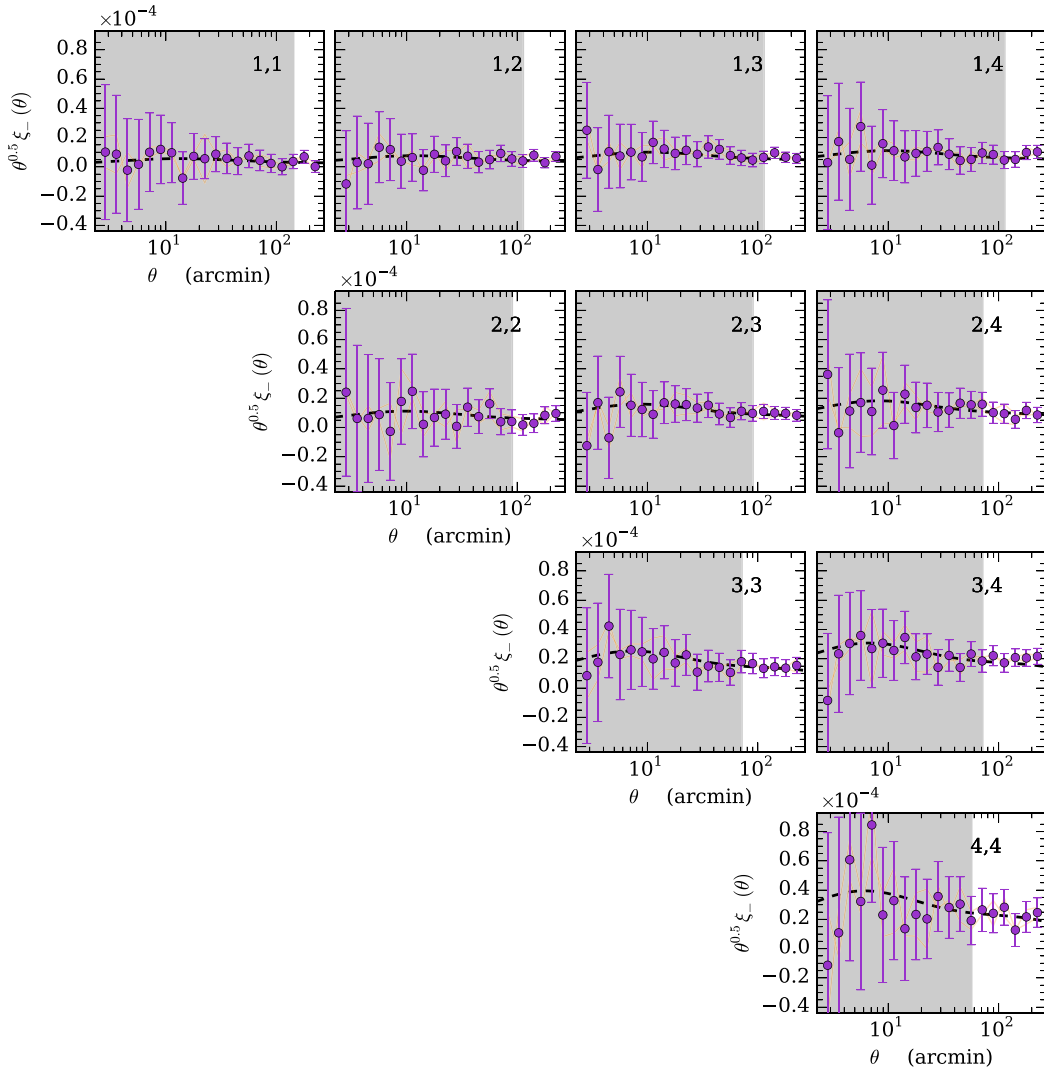
Figure A6. Measurement of $\xi_-(\theta)$ in the MICE simulations. Dark orchid data points are the mean across the two DES Y1 realizations, while orange lines indicate measurements from individual realizations. Errorbars indicate the expected uncertainty from a single DES Y1 realization. The line is the theoretical prediction assuming the true cosmology. Grey-shaded regions are excluded from the fiducial analysis.

Figure A7. Measurement of $\gamma_t(\theta)$ in the MICE simulations. Dark orchid data points are the mean across the two DES Y1 realizations, while orange lines indicate measurements from individual realizations. Errorbars indicate the expected uncertainty from a single DES Y1 realization. The line is the theoretical prediction assuming the true cosmology. Grey-shaded regions are excluded from the fiducial analysis.
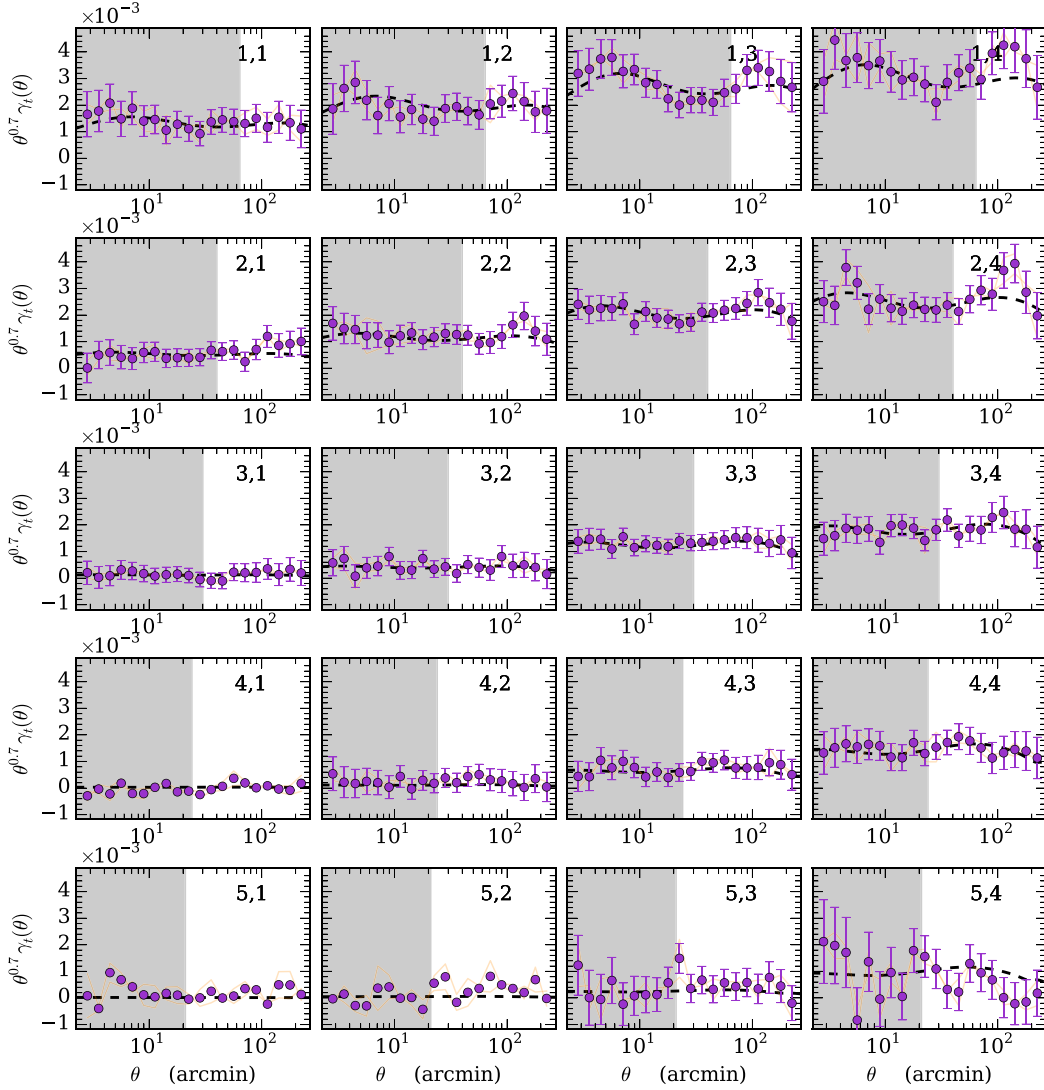

Figure A8. Measurement of $w(\theta)$ in the MICE simulations. Dark orchid data points are the mean across the two DES Y1 realizations, while orange lines indicate measurements from individual realizations. Errorbars indicate the expected uncertainty from a single DES Y1 realization. The line is the theoretical prediction assuming the true cosmology. Grey-shaded regions are excluded from the fiducial analysis.
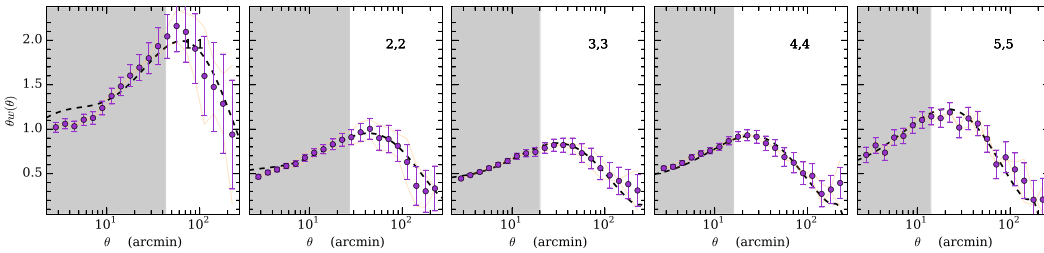
[1] *Center for Cosmology and Astro-Particle Physics, The Ohio State University, Columbus, OH 43210, USA*

[2] *Department of Physics, The Ohio State University, Columbus, OH 43210, USA*

[3] *Department of Physics, Stanford University, 382 Via Pueblo Mall, Stanford, CA 94305, USA*

[4] *Kavli Institute for Particle Astrophysics & Cosmology, PO Box 2450, Stanford University, Stanford, CA 94305, USA*

[5] *SLAC National Accelerator Laboratory, Menlo Park, CA 94025, USA*

[6] *Institute of Physics, Laboratory of Astrophysics, École Polytechnique Fédérale de Lausanne (EPFL), Observatoire de Sauverny, 1290 Versoix, Switzerland*

[7]*Institut d'Estudis Espacials de Catalunya (IEEC), E-08193 Barcelona, Spain*

[8]*Institute of Space Sciences (ICE, CSIC), Campus UAB, Carrer de Can Magrans, s/n, E-08193 Barcelona, Spain*

[9]*Department of Physics and Astronomy, University of Pennsylvania, Philadelphia, PA 19104, USA*

[10]*Steward Observatory, Department of Astronomy/, 933 North Cherry Avenue, Tucson, AZ 85721-0065, USA*

[11]*Jet Propulsion Laboratory, California Institute of Technology, 4800 Oak Grove Dr., Pasadena, CA 91109, USA*

[12]*Institute for Astronomy, University of Edinburgh, Edinburgh EH9 3HJ, UK*

[13]*Jodrell Bank Center for Astrophysics, School of Physics and Astronomy, University of Manchester, Oxford Road, Manchester M13 9PL, UK*

[14]*Institut de Física d'Altes Energies (IFAE), The Barcelona Institute of Science and Technology, Campus UAB, E-08193 Bellaterra, Barcelona, Spain*

[15]*Fermi National Accelerator Laboratory, PO Box 500, Batavia, IL 60510, USA*

[16]*Department of Physics, Carnegie Mellon University, Pittsburgh, Pennsylvania, PA 15312, USA*

[17]*Kavli Institute for Cosmological Physics, University of Chicago, Chicago, IL 60637, USA*

[18]*Department of Astronomy, University of Michigan, Ann Arbor, MI 48109, USA*

[19]*Department of Physics, University of Michigan, Ann Arbor, MI 48109, USA*

[20]*Cerro Tololo Inter-American Observatory, National Optical Astronomy Observatory, Casilla 603, La Serena, Chile*

[21]*Department of Physics & Astronomy, University College London, Gower Street, London, WC1E 6BT, UK*

[22]*Department of Physics and Electronics, Rhodes University, PO Box 94, Grahamstown, 6140, South Africa*

[23]*Institute of Cosmology & Gravitation, University of Portsmouth, Portsmouth, PO1 3FX, UK*

[24]*Laboratório Interinstitucional de e-Astronomia – LIneA, Rua Gal. José Cristino 77, Rio de Janeiro, RJ-20921-400, Brazil*

[25]*Observatório Nacional, Rua Gal. José Cristino 77, Rio de Janeiro, RJ-20921-400, Brazil*

[26]*Department of Astronomy, University of Illinois at Urbana-Champaign, 1002 W. Green Street, Urbana, IL 61801, USA*

[27]*National Center for Supercomputing Applications, 1205 West Clark St., Urbana, IL 61801, USA*

[28]*Centro de Investigaciones Energéticas, Medioambientales y Tecnológicas (CIEMAT), Madrid, Spain*

[29]*Instituto de Fisica Teorica UAM/CSIC, Universidad Autonoma de Madrid, E-28049 Madrid, Spain*

[30]*Department of Physics, ETH Zurich, Wolfgang-Pauli-Strasse 16, CH-8093 Zurich, Switzerland*

[31]*Santa Cruz Institute for Particle Physics, Santa Cruz, CA 95064, USA*

[32]*Max Planck Institute for Extraterrestrial Physics, Giessenbachstrasse, D-85748 Garching, Germany*

[33]*Fakultät für Physik, Universitäts-Sternwarte, Ludwig-Maximilians Universität München, Scheinerstr. 1, D-81679 München, Germany*

[34]*Harvard-Smithsonian Center for Astrophysics, Cambridge, MA 02138, USA*

[35]*Australian Astronomical Observatory, North Ryde, NSW 2113, Australia*

[36]*Departamento de Física Matemática, Instituto de Física, Universidade de São Paulo, CP 66318, São Paulo, SP 05314-970, Brazil*

[37]*George P. and Cynthia Woods Mitchell Institute for Fundamental Physics and Astronomy, and Department of Physics and Astronomy, Texas A&M University, College Station, TX 77843, USA*

[38]*Institució Catalana de Recerca i Estudis Avançats, E-08010 Barcelona, Spain*

[39]*School of Physics and Astronomy, University of Southampton, Southampton, SO17 1BJ, UK*

[40]*Physics Department, Brandeis University, 415 South Street, Waltham, MA 02453, USA*

[41]*Instituto de Física Gleb Wataghin, Universidade Estadual de Campinas, E-13083-859, Campinas, SP, Brazil*

[42]*Computer Science and Mathematics Division, Oak Ridge National Laboratory, Oak Ridge, TN 37831, USA*

[43]*Excellence Cluster Universe, Boltzmannstr. 2, D-85748 Garching, Germany*

This paper has been typeset from a TeX/LaTeX file prepared by the author.